UNIVERSIDADE DE SÃO PAULO
Escola de Engenharia de São Carlos

Sensor Technology Development for Human Robot Interaction and Joint Misalignment Assessment

Jonathan Campo Jaimes

Tese (Doutorado) - Programa de Pós-Graduação em Engenharia Mecânica
Área de Concentração: Dinâmica e Mecatrônica

EESC · USP

UNIVERSIDADE DE SÃO PAULO
ESCOLA DE ENGENHARIA DE SÃO CARLOS

Jonathan Campo Jaimes

Sensor Technology Development for Human Robot Interaction and Joint Misalignment Assessment

São Carlos

2024

Jonathan Campo Jaimes

Sensor Technology Development for Human Robot Interaction and Joint Misalignment Assessment

Tese apresentada à Escola de Engenharia de São Carlos da Universidade de São Paulo, para obtenção do título de Doutor em Ciências - Programa de Pós-Graduação em Engenharia Mecânica.

Área de concentração: Dinâmica e Mecatrônica

Advisor: Prof. Dr. Adriano Almeida Gonçalves Siqueira

VERSÃO CORRIGIDA

São Carlos

2024

Ficha catalográfica elaborada pela Biblioteca Prof. Dr. Sérgio Rodrigues Fontes da EESC/USP com os dados inseridos pelo(a) autor(a).

C76s

Campo-Jaimes, Jonathan
Sensor Technology Development for Human Robot Interaction and Joint Misalignment Assessment / Jonathan Campo-Jaimes; orientador Adriano Almeida Gonçalves Siqueira. São Carlos, 2024.

Tese (Doutorado) - Programa de Pós-Graduação em Engenharia Mecânica e Área de Concentração em Dinâmica e Mecatrônica -- Escola de Engenharia de São Carlos da Universidade de São Paulo, 2024.

1. Human-Robot Interaction Systems. 2. Human Torque Estimation. 3. Misalignment Estimation. 4. Robotic Rehabilitation. I. Título.

Eduardo Graziosi Silva - CRB - 8/8907

FOLHA DE JULGAMENTO

Candidato: Engenheiro **JONATHAN CAMPO JAIMES**.

Título da tese: "Desenvolvimento de Tecnologia de Sensores para Avaliação da Interação Humano-robô e do Desalinhamento Angular".

Data da defesa: 07/03/2024.

Comissão Julgadora	**Resultado**
Prof. Associado Adriano Almeida Gonçalves Siqueira (Orientador) (Escola de Engenharia de São Carlos/EESC-USP)	APROVADO
Prof. Titular Glauco Augusto de Paula Caurin (Escola de Engenharia de São Carlos/EESC-USP)	APROVADO
Prof. Dr. Wilian Miranda dos Santos (Universidade Estadual Paulista "Júlio de Mesquita Filho/UNESP-São João da Boa Vista)	APROVADO
Prof. Dr. Anselmo Frizera Neto (Universidade Federal do Espirito Santo/UFES)	APROVADO
Prof. Dr. Oscar Fernando Avilés Sánchez (Universidade Militar Nueva Granada/UMNG)	APROVADO

Coordenador do Programa de Pós-Graduação em Engenharia Mecânica:
Prof. Associado **Adriano Almeida Gonçalves Siqueira**

Presidente da Comissão de Pós-Graduação:
Prof. Titular **Carlos De Marqui Junior**

ACKNOWLEDGEMENTS

First, thank God for guiding me every step of the way. Enrolling at the USP has been a life-changing decision. Everything I've achieved is thanks to Him.

Big thanks to my advisor, Prof. Adriano Siqueira, for his endless patience and guidance. Thanks also for your support beyond the advice and for going through the highs and lows together.

Iara, you're like a second mom to me during my time in São Carlos. Thanks for everything you've done.

A special mention to my friends Mauricio, Andrés, Juan Carlos, Marlon, Booker, Yecid, Jhon, Gabriel, Maria José, João, Rayza, Edwin and Sebastian. Your support, especially during the tough times, was invaluable. Far from home, I felt you guys more like family than friends to me.

To everyone in the lab, thanks for being such a big part of my life during my studies. I appreciate every moment spent with you all.

Thanks you to the CAPES Foundation for the financial support during my studies.

Adriane, Thank you for your lovely company and support during this time of my studies. I am truly blessed to have you by my side.

To my cousin Dairon, a warrior in countless battles, your support has been a pillar of strength for me.

I sincerely thank my dad, Henry, and my sisters for their love and encouragement.

To my core family, my mom Marlene, my brother Cristhiam, and my grandma Agripina, I felt your love every single day. The strength you shared with me was my driving force. This one's for you. I hope I've made you proud, nonita.

And to all my other dear friends and relatives I didn't mention, I want you to know how grateful I am for your love and support during my studies.

"Clavo mi remo en el agua
Llevo tu remo en el mío
Creo que he visto una luz
Al otro lado del río."
Jorge Drexler

ABSTRACT

Jaimes, J.C. **Sensor Technology Development for Human Robot Interaction and Joint Misalignment Assessment**. 2024. 96p. Thesis (Doctor) - Escola de Engenharia de São Carlos, Universidade de São Paulo, São Carlos, 2024.

In the rapid and growing development of Robotics within the field of Assistive and Rehabilitation Technologies, the evaluation of human-robot interaction torques is not only important to ensure patient safety, increasing the control effectiveness of rehabilitation devices, but also serves as an essential tool to provide clinicians with more reliable data. However, the complexities associated with its measurement often result in detailed procedures or costly implementations. Seeking to address these challenges, this doctoral research aims to develop and evaluate new wearable sensor technologies to estimate interaction torques and angular misalignment for Human-Robot Interaction (HRI) systems. A suite of three specialized sensor systems was developed. The initial prototype, based on Fiber Optic technology, introduces the concept of differential sensor measurement. The second sensor presents an improved version of the previous one, employing resistive force sensors and the definition of a new misalignment factor. Finally, the third prototype features an array of resistive force sensors and even more refined measurement methodologies, validated with force/torque (F/T) sensors under controlled misalignment conditions. The data from the proposed sensors are combined with the Disturbance Observers (DOB) methodology, seeking to accurately estimate and evaluate human-robot interaction torques and inherent joint misalignments. Characterization and evaluation phases with healthy volunteers, considering different configurations, confirm the viability and robustness of the proposed sensor prototypes. Of the proposed sensors, the prototype with an array of resistive force sensors proved to be more accurate and with more flexibility for estimating interaction torques and misalignment.

Keywords: Human-Robot Interaction Systems, Human Torque Estimation, Misalignment Estimation; Robotic Rehabilitation.

RESUMO

Jaimes, J.C. **Desenvolvimento de Tecnologia de Sensores para Avaliação da Interação Humano-robô e do Desalinhamento Angular**. 2024. 96p. Tese (Doutorado) - Escola de Engenharia de São Carlos, Universidade de São Paulo, São Carlos, 2024.

No desenvolvimento rápido e crescente da Robótica dentro do campo das Tecnologias Assistivas e de Reabilitação, a avaliação dos torques de interação humano-robô não só tem importância para garantir a segurança do paciente, aumentando a eficácia do controle dos dispositivos de reabilitação, como também serve como ferramenta essencial para fornecer aos clínicos dados mais confiáveis. No entanto, as complexidades associadas à sua medição frequentemente resultam em procedimentos detalhados ou implementações de alto custo. Buscando enfrentar esses desafios, esta pesquisa de doutorado visa a desenvolver e avaliar novas tecnologias de sensores vestíveis para realizar a estimativa de torques de interação e desalinhamento angular para sistemas de Interação Humano-Robô (HRI). Um conjunto de três sistemas de sensores especializados foi desenvolvido. O protótipo inicial, baseado em tecnologia de Fibra Óptica, introduz o conceito de medição diferencial dos sensores. O segundo sensor apresenta uma versão aprimorada do anterior, empregando sensores resistivos de força e a definição de um novo fator de desalinhamento. Finalmente, o terceiro protótipo apresenta um arranjo de sensores resistivos de força e metodologias de medição ainda mais refinadas, validadas com sensores de força/torque (F/T) sob condições de desalinhamento controlado. Os dados dos sensores propostos são combinados com a metodologia de Observadores de Perturbação (DOB), buscando estimar e avaliar com precisão os torques de interação humano-robô e os inerentes desalinhamentos articulares. Fases de caracterização e avaliação com voluntários hígidos, considerando diferentes configurações, confirmam a viabilidade e robustez dos protótipos de sensores propostos. Dos sensores propostos, o protótipo com um conjunto de sensores resistivos de força mostrou-se mais preciso e com mais flexibilidade para a estimativa dos torques de interação e do desalinhamento.

Palavras-chave: Sistemas de Interação Humano-Robô, Estimativa de Torque Humano, Estimativa do Desalinhamento; Reabilitação Robótica.

LIST OF FIGURES

LIST OF TABLES

CONTENTS

1 INTRODUCTION

This Ph.D. thesis explores the challenges and innovations in estimating human joint torques in Human-Robot Interaction (HRI), specifically for Robotic Rehabilitation (RR). The focus is directed toward implementing Disturbance Observer (DO), a technique traditionally employed in robotic control systems to offset the destabilizing effects of input disturbances.

Therefore, the approach proposed in this thesis sets out to quantify human joint torques, treating them as input disturbances that the robotic system needs to estimate accurately. However, this research extends its application by integrating critical considerations of joint misalignment and the dynamic forces at play during HRI. Quantifying these biomechanical signals is essential not only for assessing a patient's functional capacity during task execution or training but also for enhancing the performance of the robot actuator. The innovation of this thesis lies in its unique integration of data on joint misalignment and human-robot interaction forces collected through a specially developed sensor system for assessing these physical aspects of HRI. By integrating these elements, the research aims to achieve a more precise and realistic estimation of human torque in RR situations. This approach seeks to enhance our understanding of human biomechanics in therapeutic contexts and contribute to more effective and responsive robotic rehabilitation training programs.

This research builds on previous work and introduces innovative solutions aimed at enhancing the effectiveness and safety of robotic rehabilitation. This introduction presents the motivations behind this research, its context, and the specific objectives and anticipated outcomes of this project.

1.1 Motivation

Human-robot interaction (HRI) has emerged as a very solid and dynamic field of study, reflecting the integration of robotic technologies across various domains of human life. The application areas that HRI encompasses vary from routine tasks like handling parts on manufacturing assembly lines to more complex interactions like assisting physically or socially the elderly and handicapped persons (Sheridan, 2016).

In perspective, new opportunities in HRI arise as more advanced robots and new sensing technologies become available as research tools and high-tech products, enabling the study of communication and interaction between various robotic designs and humans at different interaction levels (Dautenhahn, 2009). However, the rapid evolution of robotics and HRI also presents challenges and emerging gaps, as researchers are chasing a moving

target with new robots coming on the market and existing products being discontinued. This constant change leads to a situation where the robot technology used in one study may differ significantly from a robot used in the same research field just a few years later. Although this may lead to different findings and conclusions, alongside HRI research, safety always represents a paramount challenge (Zacharaki *et al.*, 2020).

Within this broad spectrum, Rehabilitation Robotics (RR) has emerged as a specialized area, focusing on utilizing robotic technologies to assist and rehabilitate patients. Assistance in RR typically involves supporting daily activities and specific tasks, helping patients maintain independence. On the other hand, rehabilitation focuses on restoring functions through adaptive exercises, emphasizing long-term recovery. Understanding these distinctions helps design robotic systems that support immediate needs and rehabilitative goals. Particularly significant is the role of human joint torques, essential biomechanical signals for assessing a patient's functionality during task execution or training. However, the quantification of joint torque presents inherent challenges, as it cannot be directly measured by any conventional sensor in practice (Lunenburger; Colombo; Riener, 2007). Some robotic-assisted devices, such as isokinetic dynamometers, use joint torque information to assess muscle strength (Kristensen; Stenager; Dalgas, 2017), but with the disadvantage of being relatively expensive. Due to the interaction between the mechanical characteristics of a muscle and its electrical activity, electromyography (EMG) has been a well-studied methodology to estimate the patient's torque (Staudenmann *et al.*, 2010; Lenzi *et al.*, 2012; Rifai *et al.*, 2017). Nevertheless, EMG measurement has practical limitations; for example, electrode fixation is time-consuming, calibration measurement is required, and signal processing can be complicated. In the research field of rehabilitation robotics, there is a great interest in finding alternative approaches to estimate the patient's torque.

In industrial robotics, the issue of measuring force and torque to ensure robot force compliance and transparency has been addressed by using end-effectors equipped with force/torque (F/T) sensors. These sensors are integrated into grippers to precisely measure the amount of force or torque exerted on the robot or the objects it interacts with. F/T sensors are essential in enhancing manipulator dexterity, accuracy, efficiency, and flexibility.

Their application in robotic rehabilitation is gaining traction, as evidenced by the study by (Escalante *et al.*, 2023), where an F/T sensor-based framework was utilized to yield transparency of controlled robotic assistance during walking, thereby enhancing compliance and actuator effectiveness. However, F/T sensors can be costly solutions, and their integration is not always straightforward, making their use a complex task. Therefore, this work's motivation extends to developing a low-cost sensor system that aims to provide similar benefits to those of conventional F/T sensors, thus making it more accessible and adaptable for robotic rehabilitation purposes.

Differing from the F/T sensor approach, a well-accepted approach in the design of control strategies for robotic assistance is to consider the human dynamic behavior as a source of disturbance inputs of the robotic system (Calanca; Fiorini, 2014; Calanca; Capisani; Fiorini, 2014; Jutinico *et al.*, 2017; Escalante *et al.*, 2018). From that perspective, using Disturbance Observer (DO) based techniques can help quantify human joint torques if considered as input disturbances to be estimated by the robotic system. According to (Chen *et al.*, 2000), a Disturbance Observer can be employed to achieve independent joint control in robots by treating inter-joint interactions as unknown external disturbances. Utilizing DO enhances robotic robustness against parameter variations and unmodeled dynamics and offers a cost-effective alternative to torque sensors. This enables sensorless approaches for force feedback and hybrid position/force control. Additionally, DO facilitates online reaction torque estimation for more adaptable control strategies, including monitoring and trajectory planning.

Some Disturbance Observer-based techniques have been used to estimate human joint torques in robotic rehabilitation scenarios. Some of the most relevant works were reported in (Abhishek; K., 2010; Ugurlu *et al.*, 2015; Daud *et al.*, 2017) for upper-limb torque estimation, and in (Mohammed *et al.*, 2016; Huo; Mohammed; Amirat, 2019; dos Santos; Siqueira, 2019b) for lower-limb torque estimation. However, in these works, the DO techniques actually do not use information about misalignment neither about interaction forces

1.2 Relevant Literature of Misalignment in Human-Robot Interaction

Much of current HRI research, particularly involving upper limb exoskeletons, has focused on joint misalignment and its implications. In Esmaeili *et al.* (2011), the authors emphasized the ergonomic impact of joint misalignment in anthropomorphic wrist exoskeletons. Their approach of introducing compliance in the interface via ideal springs to facilitate relative motion between the human hand and handle represents an innovative solution to reduce discomfort due to misalignment.

Furthermore, the systematic review by Mallat *et al.* (2019) on joint misalignment in powered exoskeletons underscores the challenges and needs for further research in this domain, particularly focusing on user safety and comfort. This comprehensive review highlights the advancements in wearable robotics and the ongoing challenges posed by misalignment in HRI systems.

In the context of lower limb robots, few studies such as those by Dezman *et al.* (2023), Gordon, Henderson e Vijayakumar (2018), and Zanotto *et al.* (2015) explore the effects of misalignment on user performance from the perspective of user performances, that is gait metrics, confort and metabolic costs.

The study by Sun, Shen e Rosen (2021) discusses sensor reduction in upper-limb exoskeletons, aligning with the objective of this thesis to develop a cost-effective sensor system for assessing misalignment and HRI. Their approach of using a Kalman filter to emulate full sensor performance with a reduced sensor setup could provide valuable insights for this research. Moreover, Chander *et al.* (2022) compare various methods for modeling the human-exoskeleton interface, focusing on kinetic alignment to address misalignment. Their approach, though distinct, offers a perspective that contrasts with this thesis's aim of incorporating, rather than avoiding, misalignment.

1.2.1 Disturbance Observer and Joint Misalignment

Integrating joint misalignment considerations within the DO framework for estimating human joint torques is notably underexplored. Current literature on DO often assumes a simplified human-robot dynamic model, neglecting the complexity introduced by misalignment. This research gap offers a unique opportunity for this thesis to extend the DO application by integrating joint misalignment considerations in HRI systems.

Existing studies employing Disturbance Observer strategies in Human-Robot Interaction (HRI) systems have not explicitly addressed joint misalignment. Although a few studies have explored a similar domain, their focus diverges significantly from the specific challenges presented in HRI systems. For instance, the research by Kasi *et al.* (2014) explores the use of DO in a robotic system for orthopedic drilling, where they acknowledge the role of bone misalignment. However, this application is distinct from the challenges of joint misalignment in human exoskeleton systems, which are central to this thesis. In a similar work, the study outlined in Javaid *et al.* (2024) introduces a second-order Disturbance Observer to mitigate actuator misalignment in spacecraft systems, further illustrating DO's diverse but non-overlapping applications in different contexts. These examples underscore the novelty and necessity of this thesis's focus on integrating joint misalignment considerations into DO strategies for HRI systems.

This research seeks to bridge the gap in the existing literature by integrating considerations of joint misalignment into the DO framework, enhancing the accuracy of human joint torque estimation in robotic rehabilitation. The reviewed studies offer insights into the complexities of joint misalignment and existing methodologies. However, they also highlight a significant gap in incorporating misalignment considerations into DO techniques, especially in lower limb exoskeletons and robotic rehabilitation contexts. This thesis, by developing a tailored sensor system and integrating misalignment into DO, aim to provide a novel approach that not only enhances human joint torque estimation accuracy but also contributes to more effective and comfortable robotic rehabilitation systems.

1.3 Contextualization

In (Jaimes, 2018), three DO-based approaches were developed for human torque estimation using the Anklebot, a robot device for ankle rehabilitation. The work was focused on estimating ankle torque during sitting position movements (Figure 1a). The three estimation approaches consisted of the Generalized Momentum Observer (GMO), a Kalman Filter algorithm with integral action (KF-I), and finally, a combination of the Kalman Filter algorithm and the Generalized Momentum (KF-M) (Figure 1b). These approaches considered the ankle torque, τ_h, as a disturbance input in the robotic control system. They used only information of joint angular displacement, θ, velocity measurements, $\dot{\theta}$, and the actuator torque, τ_r. The proposed approaches were tested by asking healthy voluntary users to perform isokinetic ankle movements while the robot supplied assistance torque. The estimation approaches proved to be successful for different human-robot interaction scenarios.

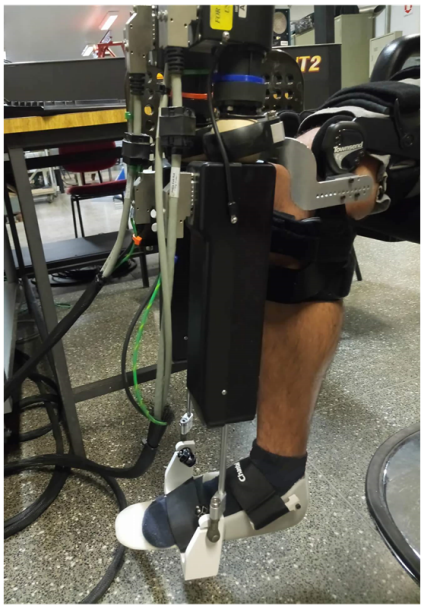

(a)

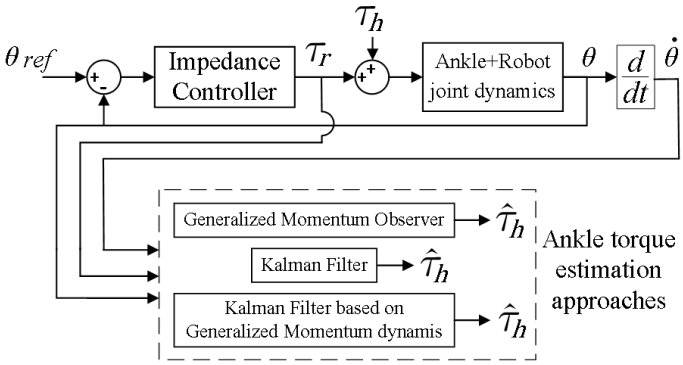

(b)

Figure 1 – The torque estimation approaches developed in (Jaimes, 2018). (a) Experimental setup using the Anklebot. (b) Schematic diagram.

The results of (Jaimes, 2018) are part of the ongoing efforts of the laboratory of Rehabilitation Robotics (ReRob Lab) at the São Carlos School of Engineering at the University of São Paulo to design novel robotic control strategies. Nevertheless, the authors of (Jaimes, 2018) are aware of the limitations during the research work. Since the Anklebot was oriented for sitting position movements, the ankle mechanical impedance parameters (inertia, damping, and stiffness) were assumed to be constant over time. If the experiments were conducted for gait training, it should have been considered that the ankle joint mechanical impedance is modulated during the gait cycle (Rouse *et al.*, 2014; Lee; Rouse;

Krebs, 2016).

Recent research at the ReRob Lab is currently studying the identification of time-varying human impedance parameters during the gait phases (Escalante *et al.*, 2020). On the other hand, work in partnership with the Telecommunications Laboratory LABTEL at the Federal University of Espírito Santo has allowed the possibility to integrate GRF measurements by using polymer optical fiber technology (Leal-Junior *et al.*, 2018a) on the robotic devices at our laboratory. Notwithstanding the preceding outcomes, challenges remained to yield a better human joint torque estimation using DO-based estimation approaches.

1.4 Research Problem

In general, the reliability of DO-based approaches relies on the level of detail of the estimation models. Nevertheless, unmodeled dynamics and nonlinearities are usually simplified on such methods to ease implementation, thereby compromising their performance. For instance, a common approach for most works is assuming that human and robot links share the same movement. However, human joint kinematics are relatively complex to emulate precisely by robotic devices; human motion is influenced by body segment variability, ligaments and tendons stretching, and inherent migration of joint centers (Rathore *et al.*, 2016). Consequently, Human-Robot Interaction (HRI) forces appear due to misalignment between robot and human joints, causing losses in the transmission of the assistive robot torques on the user's joints and leading to undesired HRI forces that can even jeopardize the safe operation. On the other hand, if the physical connections between robot and human chains were perfectly attached, kinematic incompatibility between the two systems would prevent motion. Robotic strategies are, therefore, required to have compliant behavior with admissible levels of joint misalignment and to allow operability despite kinematic discrepancies (Zanotto *et al.*, 2015).

The way DO-based estimation approaches deal with HRI forces is to lump them together with the inertial forces/torques, making the distinction between HRI forces and exogenous inputs difficult. Also, since the estimated human torques are computed using the robot kinematics information (joint angle positions and velocities), these are assumed to occur at the same axes of rotation of the robot joints. However, this does not reflect real scenarios, and the performances of DO-based estimation approaches can be affected by the unmodeled effects of joint misalignment. Thus, it becomes essential to process the torque signals caused by HRI forces to extract them from the torques the approaches estimate. This research hypothesizes that integrating information about HRI forces on DO-based observer models will improve human joint torque estimation.

The advance of sensor technology has allowed quantifying HRI forces by using

mathematical modeling (Schiele, 2008), and through the application of electronic strain gauges (ESG) (Moreno *et al.*, 2008), and load cells (Lenzi *et al.*, 2011). Polymer optical fiber (POF) sensors stand out because they offer advantages such as compactness, lightweight, chemical stability, multiplexing capabilities, and electromagnetic field immunity (PETERS, 2010). HRI force assessment with POF sensors has been developed for sitting position and gait training scenarios for robotic rehabilitation (Leal-Junior *et al.*, 2019b; Leal-Junior *et al.*, 2020). An important consideration for HRI sensors is that, during motion, high joint misalignment might shift the contact area where HRI force is being measured, thereby producing variability and unpatterned behavior of such measurements Thus, an HRI force sensor must be validated with information about joint misalignment to provide a reliable measurement.

Integrating HRI force sensors in robotic scenarios for assistance and rehabilitation purposes can also provide useful information on human performance to design robot control strategies. For instance, *human-in-the-loop* (Koller *et al.*, 2016; Zhang *et al.*, 2017) and intention-based (Kuan; Huang; Huang, 2010; Huang *et al.*, 2015; Gui; Liu; Zhang, 2017) control approaches have used HRI forces as a control variable to increase the effectiveness of the robotic assistance. However, these works neglected the joint misalignment and the quantification of HRI forces was obtained through Force Sensing Resistor (FSR) sensors, load cells, and EMG signals, letting unexplored POF sensors' alternative use.

Torque estimation using Disturbance Observers and HRI forces represents two different perspectives on detecting human joint torques in robotic-assisted scenarios. Whereas DO estimates human joint torques as exogenous inputs at the robot joints, sensors for HRI force assessment can quantify torques induced by joint misalignment that affects the estimation. Given the richness of information and the complexity of the tradeoff between DO-based estimation torque and HRI force assessment, data fusion techniques could be employed to: 1) determine by inference a correct integration of DO-based observer models with HRI force measurement to improve the human joint torque estimation and 2) recognize properly human dynamic intention/participation to design high-level robotic control strategies.

1.5 General Objective

This research aims to develop innovative techniques for estimating human joint torques, focusing on utilizing Disturbance Observer (DO) based approaches. By considering joint misalignment, human-robot interaction forces, and developing a specialized HRI sensor system, this project seeks to enhance the effectiveness, safety, and transparency of control strategies for robotic rehabilitation. These advancements are expected to contribute to studying Human-Robot interaction in the context of improving the operation of robotic systems for therapy.

To address the challenges outlined in the previous section and improve the findings of (Jaimes, 2018), this study introduces sensor technologies for estimating human joint torque and controlling high-level interactions. The following specific objectives have been established for this purpose.

- Review Current Techniques for Human Joint Torque Estimation: Analyze existing methods, particularly DO-based approaches, to identify limitations and opportunities for improvement.

- Develop a novel formulation of HRI modeling for estimation: Create a novel human joint torque estimation approach that includes information about joint misalignment and human-robot interaction forces.

- Create Sensor Systems to Assess Misalignment and Physical HRI: Design and implement specialized sensor systems that provide insights into joint misalignment and the dynamics of human-robot collaboration.

- Evaluate the Safety and Effectiveness of the Proposed Solutions: Conduct comprehensive testing and evaluation of the developed techniques and tools, considering both technical performance and user experience.

Figure 2 depicts a schematic diagram of the proposed strategy for HRI and joint misalignment assessment.

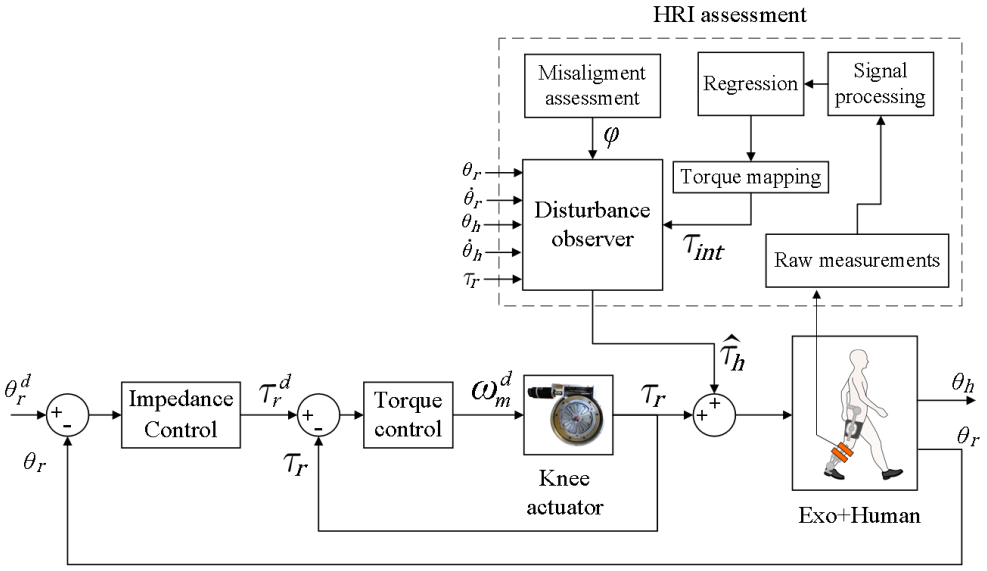

Figure 2 – Proposed HRI and misalignment assessment strategy.

1.6 Contributions

The research presented in this Ph.D. thesis comprises the following contributions to the research field of Human-Robot Interaction (HRI), particularly in estimating human joint torques for Robotic Rehabilitation (RR).

- Development of Comprehensive Torque Estimation Techniques: The thesis introduces a novel formulation for estimating human joint torques, improving upon existing Disturbance Observer (DO) based approaches. This innovative method considers better system modeling, including information about joint misalignment and human-robot interaction forces.
- Creation of Sensor Systems for HRI and Joint Misalignment Assessment: Three specialized sensor systems have been developed to assess joint misalignment and physical HRI. These systems provide valuable insights into the dynamics of human-robot collaboration, enhancing the safety and effectiveness of control design in robotic rehabilitation.
- Low-cost solution for knee joint angle estimation: The research presents a cost-effective solution for estimating knee joint angles. The development offers a practical approach to precise angle estimation by utilizing sleeve knee braces instrumented with flexible sensors, contributing to the broader accessibility of RR technologies (Appendix B).

1.7 Overview of the Proposed Sensor System Prototypes

This section provides a brief overview of the proposed sensor systems for Human-Robot Interaction (HRI), providing an initial understanding of the technological aspects and design methodologies that will be explored in detail in the following chapters.

The first prototype uses Polymer Optical Fiber (POF) technology and introduces the concept of interaction force measurement at differential contact points. The second prototype uses the same concept as the first, measuring interaction with Force Resistive Sensors and introducing a novel misalignment factor. Finally, the third prototype is built on an array of Force Resistive Sensors (FSR) and benefits from validation through an F/T sensor under adjustable misalignment configurations. Table 1 summarizes the key features of these prototypes.

1.8 Publications

During the development of this thesis, the author published the following papers as first author, such works are directly related to the work presented here:

Table 1 – Review of sensor system prototypes

Feature	**First Prototype** (Chapter 3)	**Second Prototype** (Chapter 4)	**Third Prototype** (Chapter 5)
Sensor type	POF	FSR	FSR
Interacton force Concept	Differential contact points	Differential contact points	Array contact points
Regression of HRI forces	Polynomial functions	Polynomial functions	Neural networks
Reference force sensor	Load cell	Load cell	F/T sensor
Experimental Setup	ExoTAO for walking trials	EICoSI for walking trials	Rotary SEA with adjustable misalignment

- Jonathan Campo Jaimes and Adriano Almeida Gonçalves Siqueira, Estimativa de torque para reabilitação robótica de membros inferiores: prova de conceito, in *International Workshop on Assistive Technology (IWAT2019)*, 2019.

- Jonathan Campo Jaimes, Arnaldo G. Leal-Junior, Adriano A. G. Siqueira, and Anselmo Frizera, "Instrumentation and validation of polymer optical fiber sensor technology on a knee exoskeleton," in *2019 SBMO/IEEE MTT-S International Microwave and Optoelectronics Conference (IMOC)*, pp. 1-3, 2019.

- Jonathan C. Jaimes and Adriano A.G. Siqueira, "Preliminary Evaluation of Disturbance Torque Estimation Approaches for Lower-limb Robotic Rehabilitation," in *2019 IEEE 16th International Conference on Rehabilitation Robotics (ICORR)*, pp. 715-720, 2019.

- Jonathan Campo Jaimes, Gabriel Wolschick de Oliveira, and Adriano Almeida Gonçalves Siqueira, "Sistema vestível para monitoramento da atividade física," in *XII Congreso Iberoamericano de Tecnologías de Apoyo a la Discapacidad IBERDISCAP2023*, 2023.

- Jonathan C. Jaimes, Gabriel Patti Coelho, and Adriano Almeida Gonçalves Siqueira, "Assessing the Joint Misalignment Effects in Rehabilitation Robotics: A Case Study," in *27 TH International Congress of Mechanical Engineering - COBEM Florianopolis*, 2019.

There are other conference papers and a journal article in which the author collaborated as a secondary author.

- Felix M. Escalante, Andres L. Jutinico, Jonathan C. Jaimes, Marco H. Terra, and Adriano A. G. Siqueira, "Markovian Robust Filtering and Control Applied to Reha-

bilitation Robotics," in *IEEE/ASME Transactions on Mechatronics*, vol. 26, no. 1, pp. 491-502, 2021.

- Arnaldo Leal-Junior, Leticia Avellar, Jonathan Jaimes, Camilo Díaz, Wilian dos Santos, Adriano A. G. Siqueira, Maria José Pontes, Carlos Marques, and Anselmo Frizera, "Polymer Optical Fiber-Based Integrated Instrumentation in a Robot-Assisted Rehabilitation Smart Environment: A Proof of Concept," in *Sensors*, vol. 20, no. 11, 2020.

- Felix M. Escalante, Juan C. Pérez-Ibarra, Jonathan C. Jaimes, Adriano A.G. Siqueira, and Marco H. Terra, "Robust Markovian Impedance Control applied to a Modular Knee-Exoskeleton," in *IFAC-PapersOnLine*, vol. 53, no. 2, pp. 10141-10147, 2020.

- Lucca Neves Maitan, Rafael Akihiro Matumoto, Jonathan Campo Jaimes, Juan Carlos Pérez-Ibarra, and Adriano Almeida Gonçalves Siqueira, "A Foot-Mounted Wearable Device for Online Identification of Gait Phases," in *25 TH International Congress of Mechanical Engineering - COBEM Uberlândia*, 2019.

- Felix M. Escalante, Andres L. Jutinico, Jonathan C. Jaimes, Adriano A. G. Siqucira, and Marco H. Terra, "Robust Kalman Filter and Robust Regulator for Discrete-Time Markovian Jump Linear Systems: Control of Series Elastic Actuators," in *2018 IEEE Conference on Control Technology and Applications (CCTA)*, pp. 976-981, 2018.

- Andres L. Jutinico, Felix M. Escalante, Jonathan C. Jaimes, Marco H. Terra, and Adriano A. G. Siqueira, "Markovian Robust Compliance Control Based on Electromyographic Signals," in *2018 7th IEEE International Conference on Biomedical Robotics and Biomechatronics (Biorob)*, pp. 1218-1223, 2018.

2 METHODOLOGY

2.1 Modeling Human-Robot Systems

2.1.0.1 Modeling considering ideal alignment

In conventional control strategies for exoskeletons and robotic rehabilitation devices, the joint trajectories of the robot and user are typically assumed to align perfectly. Therefore, a common shared joint angle, θ, is enough to express the angular displacement of the two bodies (see Figure 3). This assumption simplifies the dynamic Modeling of the human-robot system as shown in Equation (2.1).

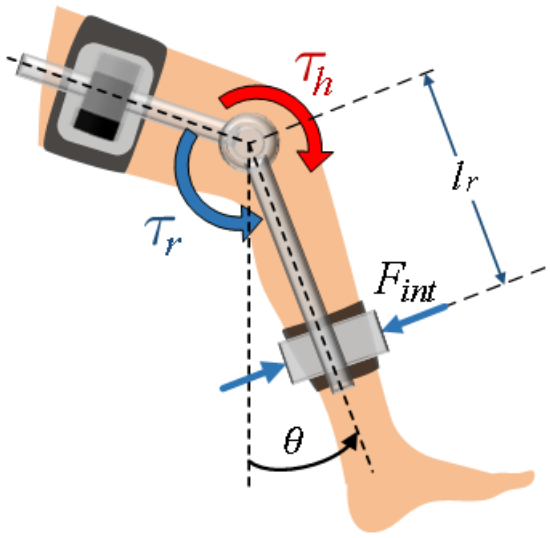

Figure 3 – Diagram considering ideal alignment in human-robot interaction

In the model, τ_r and τ_h represent the actuator and human torques, respectively, with θ being the joint angle. Interaction forces, F_{int}, occur between the human and robot at the contact surfaces, such as cuffs and straps. Under the assumption of shared movement, these forces are presumed minimal, thereby not significantly influencing the system's dynamics and kinematics. The system modeling is formulated by:

$$I_{h,r}\ddot{\theta} + B_{h,r}\dot{\theta} + K_{h,r}\theta = \tau_h + \tau_r, \tag{2.1}$$

Here, the combined dynamics of the human and robot joints are encapsulated in the impedance parameters, which include torsional inertia I, damping B, and stiffness K. In Equation (2.1), they are represented as $I_{h,r}$, $B_{h,r}$, and $K_{h,r}$, respectively. The subscripts h and r refer to the combination of the human and robot joint dynamics, i.e., $I_{h,r} = I_h + I_r$, $B_{h,r} = B_h + B_r$ and $K_{h,r} = K_h + K_r$.

2.1.1 Modeling considering misalignment

However, this idealized scenario is complicated by the presence of joint misalignment. Misalignment can lead to a loss in the effective transmission of assistive robot torques and generate unintended contact forces between human limbs and robot links. For instance, consider the knee joint flexion-extension scenario depicted in Figure 4, where interaction forces are detected at the shank cuff and leg interface using a force sensor.

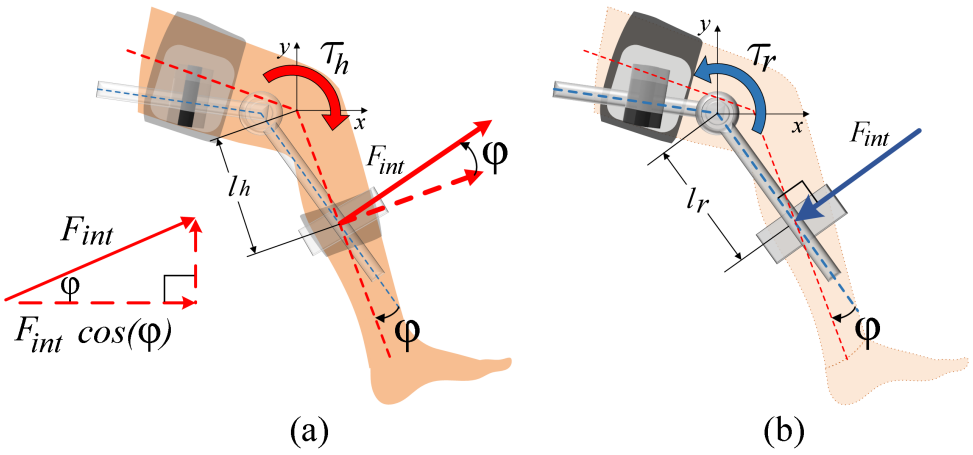

Figure 4 – Newton free bodies diagrams of a misaligned HRI scenario.
(a) Human limb. (b) Robot.

In this setup, φ represents the misalignment as the orientation angle difference between the human leg and the robot link. Consequently, the interaction torque resulting from this misalignment is differentially reflected in the human and robot joints, with lever arms l_h and l_r representing the effects of F_{int} for each side. This leads to a more complex interaction model proposed in Figure 5.

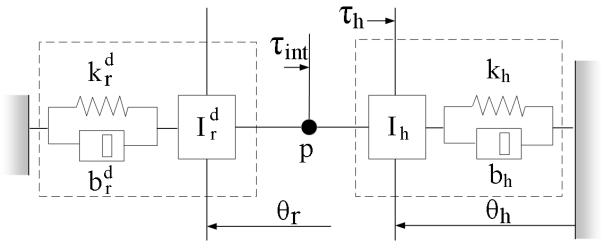

Figure 5 – Proposed human-robot coupled system.
Adapted from (Aguirre-Ollinger *et al.*, 2007)

Given that the interaction forces are detected at the surface areas of the robot cuffs and straps, the orientation of the interaction force is perpendicular to the robot link longitudinal axis. Conversely, on the human side, a Jacobian maps this force to be perpendicular to the leg's longitudinal axis. Consequently, by examining the forces for each system independently (as shown in Figure 4), the dynamic model can be reformulated as

follows:

$$I_h\ddot{\theta}_h + B_h\dot{\theta}_h + K_h\theta_h = \tau_h - \underbrace{l_h F_{int} cos(\varphi)}_{\tau_{int}}, \tag{2.2}$$

$$I_r\ddot{\theta}_r + B_r\dot{\theta}_r + K_r\theta_r = \tau_r + \underbrace{l_r F_{int}}_{\tau_{int}}. \tag{2.3}$$

The angular positions of the knee and robotic joint are denoted by θ_h and θ_r, respectively. The parameters I, B, and K represent the human and robot's inertia, damping, and stiffness, denoted with subscripts h and r. The Jacobian, $cos(\varphi)$, maps the interaction force F_{int} at the human limb side. The angle φ represents the leg and robot link misalignment.

- **Misalignment Angle Factor** φ

Consider the motion geometry shown in Figure 6 to represent the misalignment angle φ in a human-robot interaction system. The blue and red lines in the figure indicate the human and robot bodies, respectively. This misalignment occurs at the interaction port, which is the cuff surface.

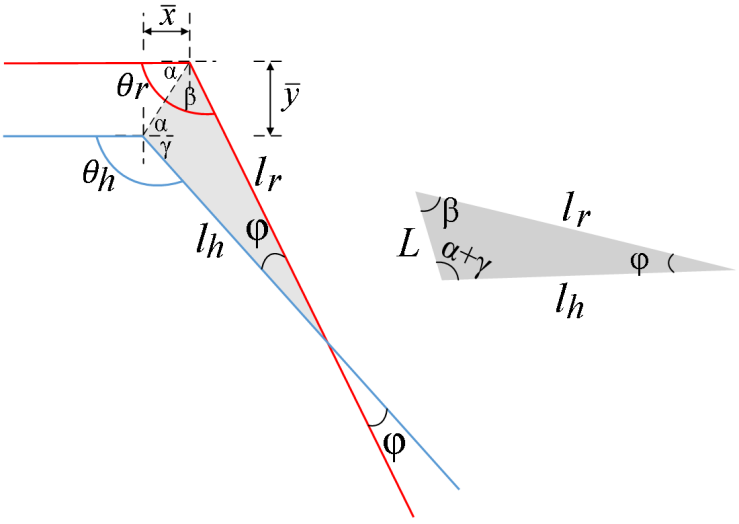

Figure 6 – Misalignment geometry.

The lever arms l_h and l_r are known parameters. The Euclidean distance between the axis of rotation of the robot and human joints is represented by L, which is given by the formula, $L = \sqrt{(x_r - x_h)^2 + (y_r - y_h)^2}$. By analyzing the axes of rotation together with the contact point at the cuff or strap, a triangle geometry can be formed, and the internal angles of the triangle can be defined as:

$$\alpha = tan^{-1}\left(\frac{\bar{y}}{\bar{x}}\right), \tag{2.4}$$

$$\beta = \theta_r - \alpha, \tag{2.5}$$

$$\gamma = 180^\circ - \theta_h, \tag{2.6}$$

Where $\bar{x}$ and $\bar{y}$ stand for the horizontal and vertical offsets of the axes of rotation, respectively, of the human and robot joints. Applying the sine law:

$$\frac{l_r}{sin(\alpha+\gamma)} = \frac{L}{sin(\varphi)}, \tag{2.7}$$

the misalignment angle φ can be computed as::

$$\varphi = sin^{-1}\left(\frac{L \cdot sin(\alpha+\gamma)}{L_r}\right). \tag{2.8}$$

2.2 Disturbance Observer-based Techniques

The fundamental concept of the Disturbance Observer (DO) (Ohnishi, 1987) lies in designing a stable linear or nonlinear dynamic system. This system, utilizing measurements from the plant as inputs, is formulated to generate an output signal linearly related to the disturbance τ_d (Sabanovic; Ohnishi, 2011). DOs have been extensively employed in robust control designs, particularly for rejecting disturbances in systems characterized by parameter uncertainties. The Disturbance Observer design involves using the inverse of the nominal plant model and developing a low-pass filter. This filter rules the system's robustness and its efficiency in disturbance rejection. Figure 7 illustrates a typical DO-based implementation for motion control, where the observer estimates an unknown external torque without relying on additional sensors.

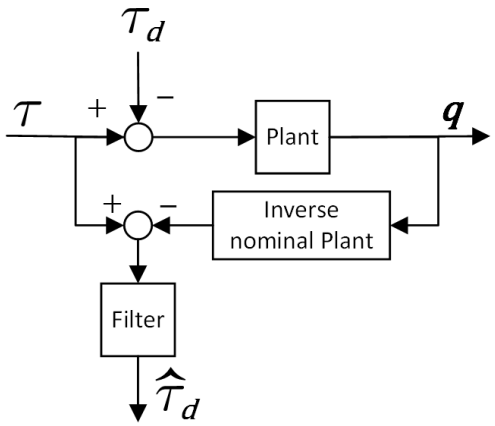

Figure 7 – Basic structure of a Disturbance Observer.
Adapted from (Sabanovic; Ohnishi, 2011)

Numerous studies have adopted the Kalman filter to devise a state observer, considering disturbances as extended system states. In this approach, disturbances are treated as additional system states. Moreover, an integrator is incorporated to align the estimated states with the actual plant states, thereby eliminating steady-state estimation errors.

This thesis delineates two principal categories of DO-based techniques. Initially, approaches that do not account for Human-Robot Interaction (HRI) are presented. These methods overlook the presence of joint misalignment and its consequent effects on the system's dynamics and kinematics. Subsequently, a novel Disturbance Observer proposal is introduced, which uniquely incorporates joint misalignment and HRI forces. This innovative approach aims to address the limitations of traditional DO techniques by integrating crucial aspects of biomechanical interactions in the modeling process.

2.2.1 Generalized Momentum Observer Approach

The generalized momenta observer approach (Van Damme *et al.*, 2011) assumes the presence of a disturbance torque (in this case τ_h) in the robotic device joints as a result of the interaction of the robot with its environment (de Luca; Mattone, 2005; De Luca *et al.*, 2006).

Consider the following dynamic model for the human-robot system:

$$I_{h,r}\ddot{\theta} + B_{h,r}\dot{\theta} + K_{h,r}\theta + \tau_g(\theta) = \tau_h + \tau_r. \tag{2.9}$$

This formulation is similar to the 1 degree of freedom (DoF) modeling of equation 2.1 but with the addition of the gravitational torque, τ_g. The idea of this approach is to observe the momentum when physical interaction between the robot and its environment occurs. Knowing that the momentum or quantity of motion of the human-robot system is defined by $p = I_{h,r}\dot{\theta}$ and its derivative by $\dot{p} = I_{h,r}\ddot{\theta}$. Thus, the dynamic Equation 2.9 can be expressed in terms of the generalized momentum as:

$$\dot{p} = \tau_r - B_{h,r}\dot{\theta} - K_{h,r}\theta - \tau_g(\theta) + \tau_h. \tag{2.10}$$

The dynamics of the momentum observer is given by

$$\dot{\hat{p}} = \tau_r - B_{h,r}\dot{\theta} - K_{h,r}\theta - \tau_g(\theta) + K_I e, \tag{2.11}$$

where $\hat{p}$ is a predictor of the momentum dynamics, K_I is a positive gain, and $e = p - \hat{p}$ is the prediction error of the momentum. By defining a residual term as $r = K_I e$, and by combining it with (2.10) and (2.11), we obtain

$$\dot{r} = K_I(\dot{p} - \dot{\hat{p}}) = K_I\tau_h - K_I r. \tag{2.12}$$

Applying Laplace to Eq. (2.12) we obtain,

$$r(s) = \frac{K_I}{s + K_I}\tau_h(s). \tag{2.13}$$

Thus, the residual term, r, is the result of applying the disturbance torque through a first-order low pass filter, namely, r is a smoothed estimate version of τ_h, i.e. $r = \hat{\tau}_h$, K_I represent the cut-off frequency. The adjustment of K_I implies a compromise between the amplitude and phase of the filtered signal r, i.e., the higher the gain, the larger the amplitude, and conversely, the lower the gain, the more significant the phase shift.

2.2.2 Kalman Filter based Disturbance Observers

Kalman filters have been used in control dynamics for either rejection or compensation disturbance estimation. Here, the state space is augmented with a dynamic disturbance model. For the specific application of the techniques developed in this thesis, a dynamic model describing the nature of the human torque viewed as a disturbance for the robotic system will be introduced into the HRI modeling. The formulations presented here will be stated until state-space modelings. Their subsequent implementation will follow the discrete-time KF algorithm described in Section 2.2.2.5

2.2.2.1 Sinusoidal disturbance model

Let's assume that human joint position trajectories performed in robotic-assisted training and locomotion analysis are patterned signals that sinusoidal equations can describe. Hence, the mathematical model generating such signals is given by the following sum of the sine function:

$$\theta^d(t) = \sum_{n=1}^{n_d} a_n \sin(\omega_n t + \phi_n), \quad t > 0, \tag{2.14}$$

Where n_d represents the number of sine functions making up the signal. The terms a_n, ω_n, and ϕ_n stand for the amplitude, frequency, and phase, respectively. The frequency is expressed in rad/s, that is, $\omega_n = 2\pi f_n$, where f_n is the frequency in Hertz of the n-th element. For a case of $n_d = 1$, i.e. a pure sine, the disturbance model is given by:

$$\underbrace{\begin{bmatrix} \ddot{\tau}_d \\ \dot{\tau}_d \end{bmatrix}}_{\dot{x}_{d_{(2n_d \times 1)}}} = \underbrace{\begin{bmatrix} 0 & -\omega_n^2 \\ 1 & 0 \end{bmatrix}}_{A_{d_{(2n_d \times 2n_d)}}} \underbrace{\begin{bmatrix} \dot{\tau}_d \\ \tau_d \end{bmatrix}}_{x_{d_{(2n_d \times 1)}}}, \tag{2.15}$$

where A_d represents the state-space model of the disturbance model.

2.2.2.2 KF and sinusoidal disturbance for the HRI aligned system

The system dynamics (Eq. 2.9) and the state-space representation of the sinusoidal disturbance model (Eq. 2.15) can be arranged to give the following augmented state-space system:

$$\underbrace{\begin{bmatrix} \ddot{\theta} \\ \dot{\theta} \\ \dot{x}_{d_{(2n_d\times 1)}} \end{bmatrix}}_{\dot{x}} = \underbrace{\begin{bmatrix} -\frac{B_{h,r}}{I_{h,r}} & -\frac{K_{h,r}}{I_{h,r}} & 0_{(1\times 2n_d-1)} & -\frac{1}{I_{h,r}} \\ 1 & 0_{(2n_d+1\times 1)} & 0_{(1\times 2n_d)} & \\ 0_{(2n_d\times 1)} & & A_{d_{(n_d\times n_d)}} & \end{bmatrix}}_{A_c} \underbrace{\begin{bmatrix} \dot{\theta} \\ \theta \\ x_{d_{(2n_d\times 1)}} \end{bmatrix}}_{x}$$
$$+ \underbrace{\begin{bmatrix} \frac{1}{I_{h,r}} \\ 0_{(2n_d+1\times 1)} \end{bmatrix}}_{B_c} \underbrace{(\tau_r - \tau_f(\dot{\theta}) - G(\theta))}_{u}, \tag{2.16}$$

$$y = \underbrace{\begin{bmatrix} I_{(2\times 2)} & 0_{(2n_d\times 2)} \\ 0_{(2\times 2n_d)} & 0_{(2n_d\times 2n_d)} \end{bmatrix}}_{H} \underbrace{\begin{bmatrix} \dot{\theta} \\ \theta \\ x_{d_{(2n_d\times 1)}} \end{bmatrix}}_{x}, \tag{2.17}$$

the terms A_c and B_c stand for the augmented continuous state transition and input matrices, H is the measurement gain matrix, and x and u are the augmented state and input vectors, respectively. Since the standard Kalman filter is designed for linear systems, the gravitational and friction torques are included in the input, u, instead of the state transition matrix, A_c.

2.2.2.3 KF and sinusoidal disturbance for the HRI misaligned system

This Kalman Filter uses a state-space arrangement from equations 2.2 and 2.3. Following the structure of a dynamic linear state-space system given by:

$$\dot{\mathbf{x}} = \mathbf{A}\mathbf{x} + \mathbf{B}\mathbf{u}, \tag{2.18}$$

$$\mathbf{y} = \mathbf{C}\mathbf{x} \tag{2.19}$$

Then, by including τ_h as an additional state and F_{int} as an input, the state vector is defined as $\mathbf{x} = [\dot{\theta}_r, \theta_r, \dot{\theta}_h, \theta_h, \tau_h]^T$, and the input vector $\mathbf{u} = [\tau_r, F_{int}]^T$. And the system matrices are given by

$$\mathbf{A} = \begin{bmatrix} -\frac{B_r}{I_r} & -\frac{K_r}{I_r} & 0 & 0 & 0 \\ 1 & 0 & 0 & 0 & 0 \\ 0 & 0 & -\frac{B_h}{I_h} & -\frac{K_h}{I_h} & \frac{l_h\cos(\varphi)}{I_h} \\ 0 & 0 & 1 & 0 & 0 \\ 0 & 0 & 0 & 0 & A_d \end{bmatrix}, \mathbf{B} = \begin{bmatrix} \frac{1}{I_r} & \frac{l_r}{I_r} \\ 0 & 0 \\ 0 & -\frac{l_h\cos(\varphi)}{I_h} \\ 0 & 0 \\ 0 & 1 \end{bmatrix}, \mathbf{C} = \begin{bmatrix} 1 & 0 & 0 & 0 & 0 \\ 0 & 1 & 0 & 0 & 0 \\ 0 & 0 & 1 & 0 & 0 \\ 0 & 0 & 0 & 1 & 0 \\ 0 & 0 & 0 & 0 & 0 \end{bmatrix}. \tag{2.20}$$

A_d represents the dynamics of the disturbance input; in this case, τ_h is formulated as a sinusoidal model. Again, the matrix A_d in Equation 2.15 defines the dynamic behavior of the disturbance input. Specifically, A_d is structured to encapsulate a sinusoidal model, with its elements reflecting the oscillatory nature of the disturbance.

2.2.2.4 Combined Kalman Filter and Generalized Momentum Approach

This combined approach was based on the one proposed in (Wahrburg; Matthias; Ding, 2015) to estimate the external forces of a 7-DoF manipulator. The idea of this formulation is to combine the robot's generalized momentum with a disturbance model given by the following first-order model:

$$\dot{\tau_d} = A_d \tau_d + w_d, \tag{2.21}$$

where A_d determines the dynamics assumed for the disturbance, $\omega_d \sim N(0, Q_d)$ are modeling inaccuracies represented as mean zero random variables. By defining the state vector $x = [p^T \;\; \tau_d^T]^T$ and introducing the abbreviation $\bar{\tau} = \tau_r - B_{h,r}\dot{\theta} - K_{h,r}\theta - G(\theta) - \tau_f(\dot{\theta})$, Equations (2.21) and (2.10) can be rearranged to form the augmented system

$$\underbrace{\begin{bmatrix} \dot{p} \\ \dot{\tau_d} \end{bmatrix}}_{\dot{x}} = \underbrace{\begin{bmatrix} 0 & -1 \\ 0 & A_f \end{bmatrix}}_{A_c} \underbrace{\begin{bmatrix} p \\ \tau_d \end{bmatrix}}_{x} + \underbrace{\begin{bmatrix} 1 \\ 0 \end{bmatrix}}_{B_c} \underbrace{\bar{\tau}}_{u} + w. \tag{2.22}$$

The vector $w = [w_p^T \;\; w_d^T]^T$ includes the disturbance noise and not-modeled input noises, w_p. By assuming a measurement noise at the Generalized Momentum, $v \sim N(0, R)$, the output equation is given by:

$$p = \underbrace{[1 \;\; 0]}_{H} \underbrace{\begin{bmatrix} p \\ \tau_d \end{bmatrix}}_{x} + v. \tag{2.23}$$

2.2.2.5 Kalman Filter algorithm implementation

The following KF discrete algorithm is implemented based on the presented in (S; Angus, 2014). Since the above state space formulation models featured nonlinear components, they can be expressed as:

$$\dot{x} = f(x(t), u(t), t), \tag{2.24}$$

where linearization of the process model around an equilibrium point $\bar{x}$, satisfying $f(\bar{x}, \bar{u}) = 0$ with $\bar{u}$ as the equilibrium input, yields constant matrices:

$$A = \left.\frac{\partial f}{\partial x}\right|_{x=\bar{x},u=\bar{u}}, \quad B = \left.\frac{\partial f}{\partial u}\right|_{x=\bar{x},u=\bar{u}}. \tag{2.25}$$

The linearized model's transition matrix A is updated using the most recent state estimate at each step. This model is then discretized into a time-varying, discrete-time linear system:

$$x_k = A_k x_{k-1} + B_k u_k + w_{k-1}, \tag{2.26}$$

$$z_k = H x_k + v_k. \tag{2.27}$$

This discrete Kalman filter addresses the problem of estimating the state $x \in \mathbb{R}^n$ of a discrete-time controlled process governed by the linear stochastic difference equation above, with a measurement $z \in \mathbb{R}^m$.

The process and measurement noise, represented by w_k and v_k respectively, are assumed to be independent, white, and normally distributed:

$$p(w) \sim N(0, Q), \tag{2.28}$$

$$p(v) \sim N(0, R). \tag{2.29}$$

where Q and R are the noise covariance matrices for the process and measurement.

The Kalman filter employs a two-step process: the *time update* equations project forward the current state and error covariance estimates to obtain *a priori* estimates, while the *measurement update* equations incorporate new measurements to refine these estimates into *a posteriori* estimates:

$$\hat{x}_k^- = A\hat{x}_{k-1} + Bu_k, \tag{2.30}$$

$$P_k^- = AP_{k-1}A^T + Q, \tag{2.31}$$

$$K_k = P_k^- H^T (HP_k^- H^T + R)^{-1}, \tag{2.32}$$

$$\hat{x}_k = \hat{x}_k^- + K_k(z_k - H\hat{x}_k^-), \tag{2.33}$$

$$P_k = (I - K_k H)P_k^-. \tag{2.34}$$

Each cycle of time and measurement updates enhances the process state's estimation, leveraging feedback to continually refine system predictions and adjustments.

2.3 Sensors for HRI system prototyping

This section reviews the Polymer Optical Fiber (POF) and Force-Sensitive Resistor (FSR) sensors selected for prototyping the HRI sensor systems. Each sensor offers distinct benefits and challenges when designing prototypes.

2.3.1 Polymer Optical Fiber Sensors

This section synthesizes contributions from (Leal Junior; Frizera; Pontes, 2017; Leal-Junior *et al.*, 2018a; Leal-Junior *et al.*, 2019b; Leal-Junior *et al.*, 2019a; Leal-Junior *et al.*, 2020) on the development and application of polymer optical fiber (POF) sensors in healthcare devices. POF sensors, particularly those based on intensity variation, are notable for their low-cost and effective modulation of optical power loss in response to physical changes. These sensors measure the attenuation of light transmitted through the fiber when it undergoes bending due to physical stresses like temperature and pressure (see Figure 8). Sensor sensitivity and linearity are enhanced by creating a polished, sensitive zone on the bent fiber.

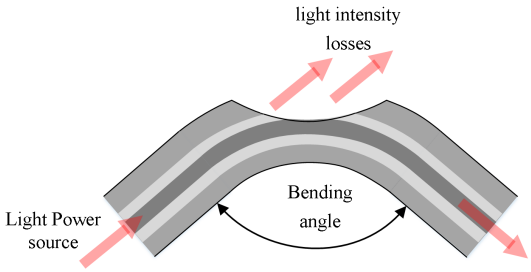

Figure 8 – Principle of operation of POF sensor.
Adapted from: (Leal Junior; Frizera; Pontes, 2017)

The instrumentation for these sensors is straightforward when working with light power amplitude, involving only a light source, optical fibers, and a photodetector. However, if the measurement involves analyzing the frequency domain, the instrumentation becomes more complex due to the need for techniques and signal processing equipment such as a spectrum analyzer. The bending geometry influences the attenuation in the sensitive zone due to the loss of cladding and increased radiation losses, leading to a model that combines geometrical optics with viscoelastic models for dynamic bending (Leal Junior; Frizera; Pontes, 2017).

A practical application of these sensors for human-robot interaction (HRI) forces assessment is seen in (Leal-Junior *et al.*, 2019b), where a 3D-printed shank support is instrumented with POF sensors designed to assess the forces. The sensors embedded in flexible thermoplastic polyurethane (TPU) structures detect force by curvature changes in the fiber, indicating power attenuation (see Figure 9a). Calibrated tests under controlled environmental conditions validated the sensors, showing variations in force sensitivity related to changes in temperature and humidity, highlighting the need for compensation in sensor response.

In (Leal-Junior *et al.*, 2020), an integrated POF sensor system was developed to monitor biosignals in lower limb wearable devices during robotic rehabilitation, incorporating multiplexing techniques to handle multiple sensor inputs across varied therapeutic

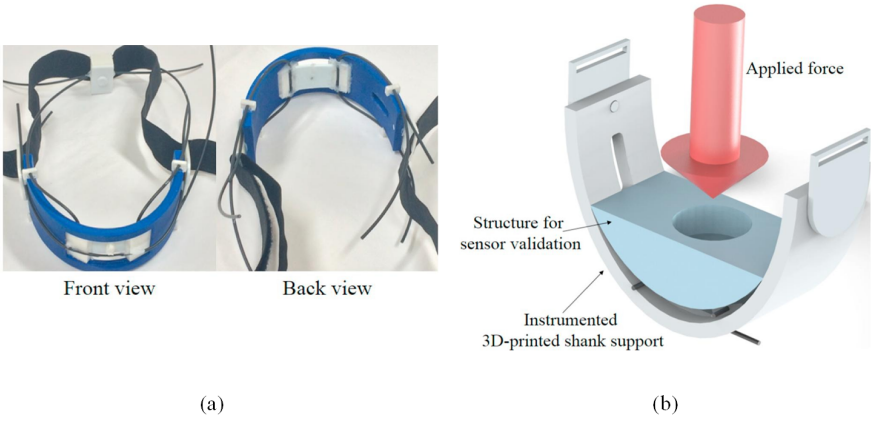

Figure 9 – POF sensor for HRI assessment
from (Leal-Junior *et al.*, 2019b): (a) Prototype views, (b) Validation setup.

scenarios.

Despite the advantages, POF sensors face significant challenges. The viscoelastic nature of the polymers used can affect the sensors' response dynamics, necessitating advanced signal processing techniques to ensure accuracy, especially under dynamic conditions (Rahuman *et al.*, 2023). Sensitivity to mechanical stresses and environmental conditions can also lead to signal degradation over time, potentially reducing the sensors' operational lifespan and reliability.

2.3.2 Force Sensitive Resistor Sensors

Force Sensitive Resistors (FSRs) are pivotal in the design of rehabilitation robotic systems and human-robot interaction due to their affordability and adaptability. FSRs are primarily utilized to measure normal forces within compact designs of wearable devices and robotic interfaces. In robotic exoskeletons, FSRs have been used for monitoring and controlling interaction forces to align with user intentions, (Huo *et al.*, 2010). These sensors are featured in various prototypes to refine device control and ensure user safety through accurate force measurement at the human-device interface (Bessler *et al.*, 2019; Dianchun *et al.*, 2014). Additionally, innovative applications like force-sensing handles demonstrate how FSRs can reduce required force in therapy sessions, improving both effectiveness and comfort (Erwin *et al.*, 2013).

Despite their advantages, FSRs exhibit several limitations that affect their reliability and performance. The non-linear response and variable transfer functions of FSRs necessitate frequent calibration to maintain accuracy (Bessler-Etten *et al.*, 2024; Grosu *et al.*, 2017). Additionally, their sensitivity to environmental factors and susceptibility to rapid degradation demand ongoing maintenance to ensure consistent functionality. The placement and configuration of FSRs are critical; improper setups can lead to significant variances in measurement accuracy, as highlighted by varying outcomes across different applications and setups (Grosu *et al.*, 2017).

2.3.3 Overview of Sensors

Table 2 compares the technological attributes, advantages, limitations, and applications of POF and FSR sensors in rehabilitation robotics.

Table 2 – Comparison of POF and FSR Sensors in Rehabilitation Robotics

Aspect	**Polymer Optical Fiber (POF) Sensors**	**Force Sensitive Resistor (FSR) Sensors**
Technology	Light attenuation due to fiber bending, high flexibility, and immunity to electromagnetic interference.	Changes in resistance under pressure, compact, easy integration.
Typical Applications in RR	Joint motion tracking, gait analysis, posture assessment, gait phase and GRF identification.	Grip strength, interaction force feedback, pressure mapping, gait phase, and GRF identification.
Advantages	Electromagnetic noise immunity, high sensitivity.	Cost-effective, simple to use.
Limitations	Requires complex signal processing when working in the frequency domain, sensitive to environmental changes.	Nonlinear, frequent calibration needed, rapid degradation.

2.4 Robotic Devices

2.4.1 Modular exoskeleton Exo-TAO

The Exo-TAO (dos Santos; Siqueira, 2019a) is a modular lower limb exoskeleton (Fig. 1) designed to allow an easy and fast coupling of different actuators. The exoskeleton can assist using an active device, such as a motor coupled to a gearbox, or a passive device, such as springs and dampers. The mechanical joints are designed to cover all ranges of motion required for different tasks. The maximum range of motion is $\pm 120°$. However, it can be limited by adjustable end-stops to prevent joint hyperextension.

The exoskeleton joints have absolute encoders (AksIMTM manufactured by RLS Company) to measure joint angular positions. Due to its modularity, the device can be actuated from any of its joints. The control system for the exoskeleton actuators controllers is structured into two main levels: a Force/Torque Control, which deals with human and robot dynamics to ensure high performance and stability despite the system's uncertainties and external disturbances, and an Impedance Control in charge of regulating the dynamic relationship between the robot's end-effector velocity and force, utilizing a proportional-derivative (PD) position controller to modify the robot stiffness and damping, ensuring compliant interaction with users.

Figure 10 – Modular Lower Limb Exoeskeleton Exo-TAO

2.4.2 Knee Rotary Series Elastic Actuator

The rotary Series Elastic Actuator (SEA) (dos Santos; Caurin; Siqueira, 2017) is a one-degree-of-actuator with a 150W DC motor (Maxon RE40) controlled using an EPOS 24/5 electronic board. The SEA's design, characterized by a rotary spring with stiffness of 105 Nm/rad, provides the necessary elasticity and resilience, ensuring smooth and adaptive interaction with the user's movements.

Figure 11 – The Rotary SEA.
(dos Santos; Caurin; Siqueira, 2017)

2.4.2.1 Setup to adjust joint misalignments

The experimental setup was designed to offer a controlled environment where misalignment could be safely and accurately adjusted. This approach ensured that the experiments were conducted reliably and securely, which is essential for validating the interaction forces and the system's response to varying degrees of misalignment. The rotary SEA was mounted on an adjustable aluminum structure, enabling precise configuration

of the robot joint's position. This structure facilitated shifts in the robot joint along the x-axis and y-axis, allowing controlled deviations in the rotation axis within the Cartesian plane.

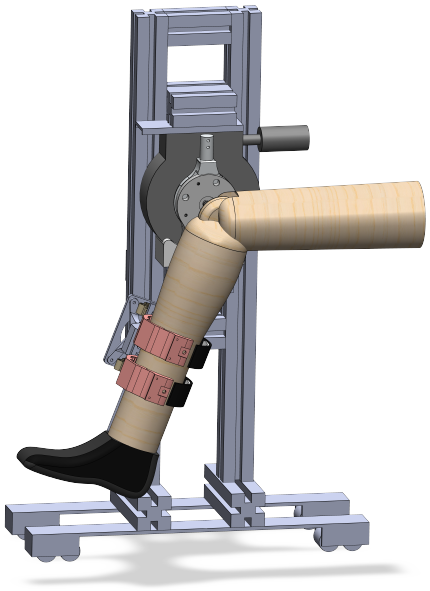

Figure 12 – Rotary SEA setup for experiments

Users wearing the mechanical setup sit in a wooden chair with their right leg coupled to the robotic actuator, which offers knee rotation in flexion and extension movements. The thigh leg is then hung so that the knee joint performs unobstructed forward and backward movements. The robotic joint is aligned with the user's knee height. Movements are conducted in the sagittal plane (XY plane). The user's leg is secured to the robot arm via a contact interface, where the physical interaction occurs.

Table 3 – Misalignment Configurations

Configuration	Displacement in X direction	Displacement in Y direction
Alignment	0	0
Misalignment 1	$50mm$	0
Misalignment 2	$-50mm$	0
Misalignment 3	0	$50mm$
Misalignment 4	0	$-50mm$

The Rotary SEA setup allows five misalignment configurations (Figure 13), each uniquely altering the robot's joint position relative to the user's knee. Configurations ranged from close alignment to various displacements along the X and Y axes (Misalignments 1 to 4), as summarized in Table 3. The adjustments were visually inspected, supported by an Infrared (IR) Laser system for precise alignment.

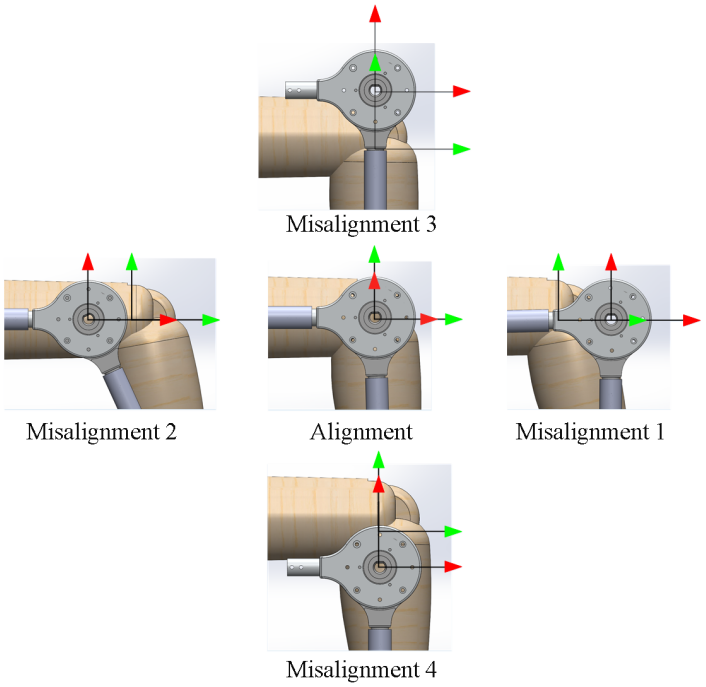

Figure 13 – Misaligment configurations using the Rorary SEA setup

2.4.3 The EICoSI knee exoskeleton

The EICoSI knee exoskeleton (Rifai *et al.*, 2017) (Figure 14), is a powered knee orthosis actuated by a compact brushless DC motor (BLDC motor). It was chosen for its high dynamic performance, lightweight nature, effectiveness at low frequency, robustness, reliability, high torque output, and reduced obstruction factor. The exoskeleton employs a dSPACE DS1103 controller board to calculate the control assistance torque, and the entire actuator can generate a maximum torque of 18 Nm. The actuator joint angle is determined by the incremental encoder installed in the exoskeleton. The device comprises two segments that can be attached to the wearer's thigh and shank region using straps and is worn on the user's right leg.

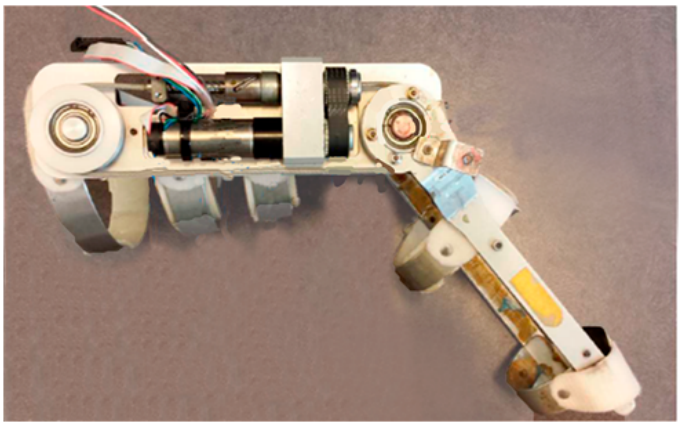

Figure 14 – The EICoSI knee exoskeleton.
(Rifai *et al.*, 2017)

2.4.4 Reference signal for validation of estimations

Unlike the ideal alignment scenario, this formulation distinguishes between interaction and human torque. Then, it can be assumed that the left side of equation 2.2 represents the passive component of the human torque denoted by $\tau_{h_{pas}}$, then the human joint torque can be approximated as $\bar{\tau}_h$, as follows:

$$\underbrace{I_h\ddot{\theta}_h + B_h\dot{\theta}_h + K_h\theta_h}_{\tau_{h_{pas}}} = \tau_h - \underbrace{l_h F_{int} cos(\varphi)}_{\tau_{int}},$$

$$\bar{\tau}_h = \tau_{h_{pas}} + \tau_{int} \tag{2.35}$$

If there is no misalignment, the lever arms at the contact point would be equal, and the angles could be considered the same. Under these conditions, Equations 2.2 and 2.3 can be combined, eliminating the interaction force and returning to the ideally aligned model presented in Equation 2.1.

3 POF-BASED SENSOR DEVICE FOR ASSESSMENT OF HRI FORCES AND JOINT MISALIGNMENT

3.1 Principle of Operation

This prototype uses POF technology to construct a POF system for HRI force and joint misalignment assessment. This proposal adapts the sensor developed in (Leal-Junior *et al.*, 2019b). The POF system design embeds an arrangement of 4 optical fibers in a double 3D-printed shank cuff. The fibers are arranged so they provide interaction force measurement at four different places of the leg. Figure 15a shows a schematic representation of the sensor arrangement; this is a lateral view of the sensor placed on a human-exoskeleton scenario.

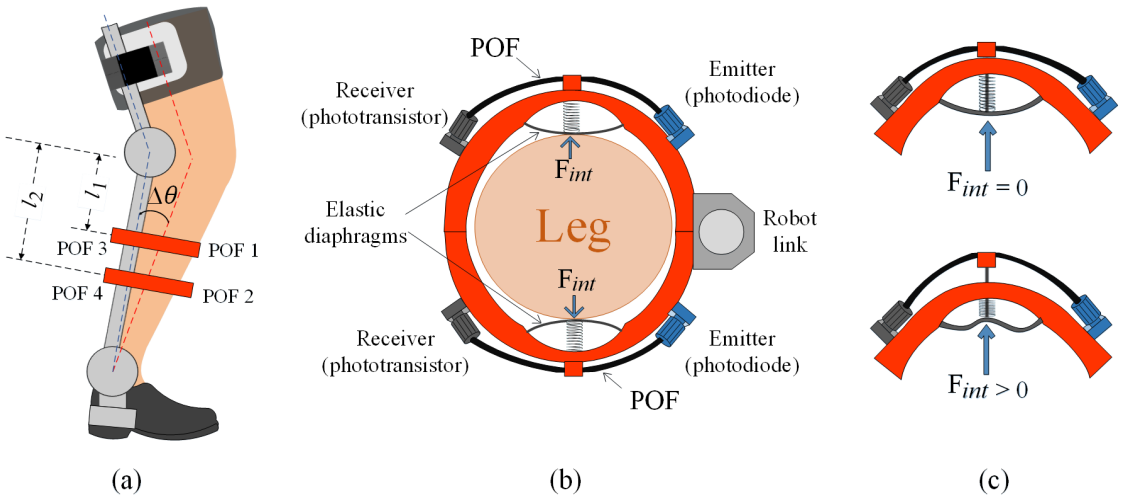

Figure 15 – POF sensor system design
(a) lateral view (b) Cross-sectional view (c) Operation functioning

The sensors are distributed to detect the HRI force at the front and back of the leg and at two different distal/proximal points to the joint. Thus, POF sensors 1 and 2 target forces on the leg's front with lever arms l_1 and l_2, while sensors 3 and 4 do the same at the back. The cross-sectional view in Figure 15b shows the leg, cuff, and robot link placement. Each fiber has emitter (phototransistor) and receiver (photodiode) circuits. Given that most interaction forces occur at the front and back of the leg, a compliant mechanism comprising a spring-diaphragm set is utilized at each contact point to ensure the fiber's radius curvature is restored when not under force. Figure 16 depicts this restoring effect, where the fiber returns to its equilibrium position when $F_{int} = 0$, indicating no interaction force.

The POF sensors provide individual force readings, with the total HRI force reflected as torque on the human or robot joint calculated through a weighted function combining these forces. Importantly, each sensor's force measurement is influenced by the

joint misalignment, $\Delta\theta$. Figure 16 elucidates the operation concept and the impact of joint misalignment on transmitted interaction forces, represented as spring elements in the sensor model. The system is designed to analyze the misalignment between human leg and robot link by evaluating the signal parameters and combinations of POF signals.

Each of the fibers will yield individual information about the interaction force. The total HRI force reflected as torque at either the human or robot joint can be obtained by processing a weighted function that compiles the interaction forces transmitted on the optical fibers. Nevertheless, each POF will give a force that is dependent on the joint misalignment, $\Delta\theta$.

The operational concept of the POF sensor system, along with its response to joint misalignment, is elucidated in Figure 16. In this figure, the forces detected by the POF sensors are conceptualized as spring elements, providing a clear visualization of the system's response to varying alignment conditions. Under ideal circumstances, where the leg and robot link are perfectly aligned, the POF sensors' signals are expected to be at minimal levels, indicating a state of equilibrium.

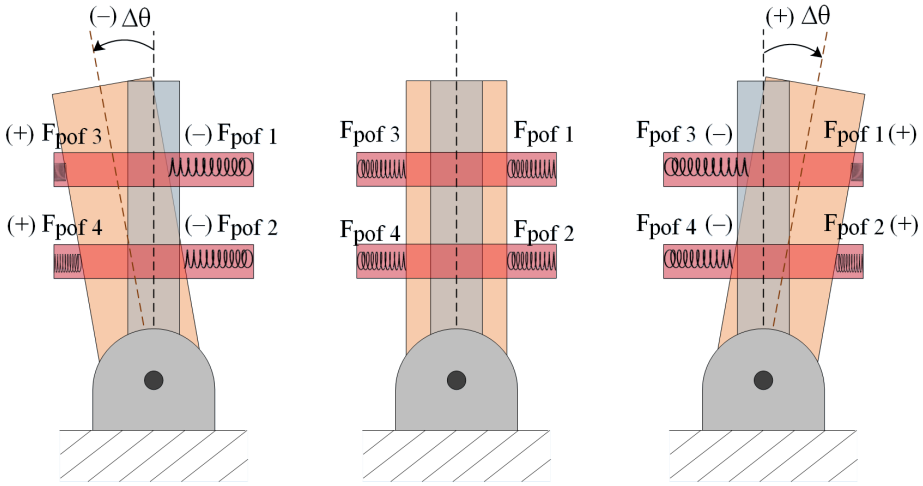

Figure 16 – POF sensor system operation concept

However, the occurrence of joint misalignment alters the sensor response significantly. This misalignment, either positive or negative based on the relative movement direction, leads to distinct compression or release patterns in the sensor pairs. Specifically, positive misalignment compresses POF sensors 1 and 2, resulting in positive signals, while simultaneously releasing sensors 3 and 4, generating negative signals. The inverse is true for negative misalignment. The differential analysis of these paired POF sensor signals offers valuable insights into the nature and degree of joint misalignment. By closely observing the variations and contrasting the signal differences between each pair (sensors 1 and 2 vs. sensors 3 and 4), meaningful conclusions about the misalignment dynamics can be observed.

3.2 Sensor Assembly

As shown in Figure 17, the prototype, an arrangement of 4 optical fibers, is embedded in a double 3D-printed shank cuff. The device is lightweight, comfortable, and adjustable to leg diameters and robot link geometries. It can also be adapted for any robot link geometry by adding tailored 3D-printed support. The diaphragm of each POF sensor, made of a small rubber sheet, is fitted onto the cuff. Two small coil springs strengthened the curvature radius restoration, one placed between the fiber and the diaphragm and the other surrounding the fiber at the photodiode´s side.

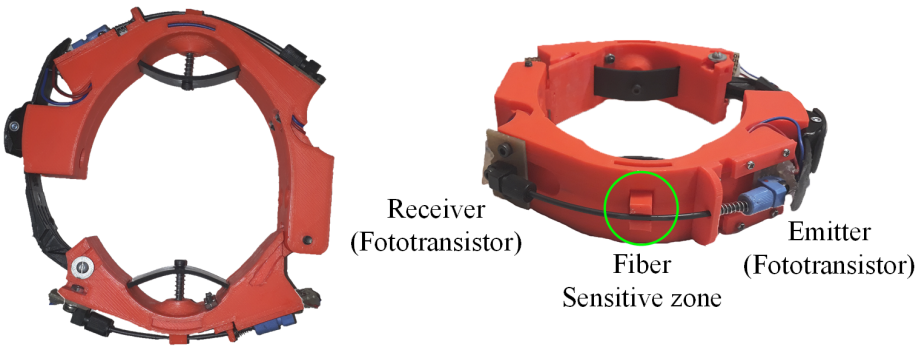

Figure 17 – POF sensor system assembly

The optical fiber employed in the sensor system is a multimode PMMA with a core diameter of 980 μm and cladding thickness of 10 μm. The cladding and part of the four fibers' core were removed at their middle lengths to form the sensitive zones. This process is done by placing the fiber in a 3D-printed support that leaves a lateral fiber zone uncovered to be removed by a rotary tool. For each of the POF sensors, the light source is provided by a Light-emitting diode IF-E97 (Industrial Fiber Optics, USA) at one end of the fiber and detected at the other end by a phototransistor IF-D92 (Industrial Fiber Optics, USA). The phototransistor circuit is fixed in the shank cuff; the photodiode circuit is placed on a sliding base to allow the curvature radius's increment and restoration.

Figure 18 shows the electric diagram of the POF sensor system. A microcontroller NodeMCU-ESP32 board was used for the data acquisition and the light power supply for POF sensors. The POF sensor system's circuits are supplied with 3.3 volts, the voltage provided by the ESP32 board. Four external 12-bit ADC modules (Adafruit ADS1015) were used for the raw signal acquisition. The modules were configured to obtain high-resolution measurements with a gain of 0.000500V/digit and a rate of 500 Hz. The electrical system incorporates humidity and temperature measurements through the DHT11 sensor. The ESP32 board sends the data information over a serial USB to a PC workstation and is analyzed using MATLAB software.

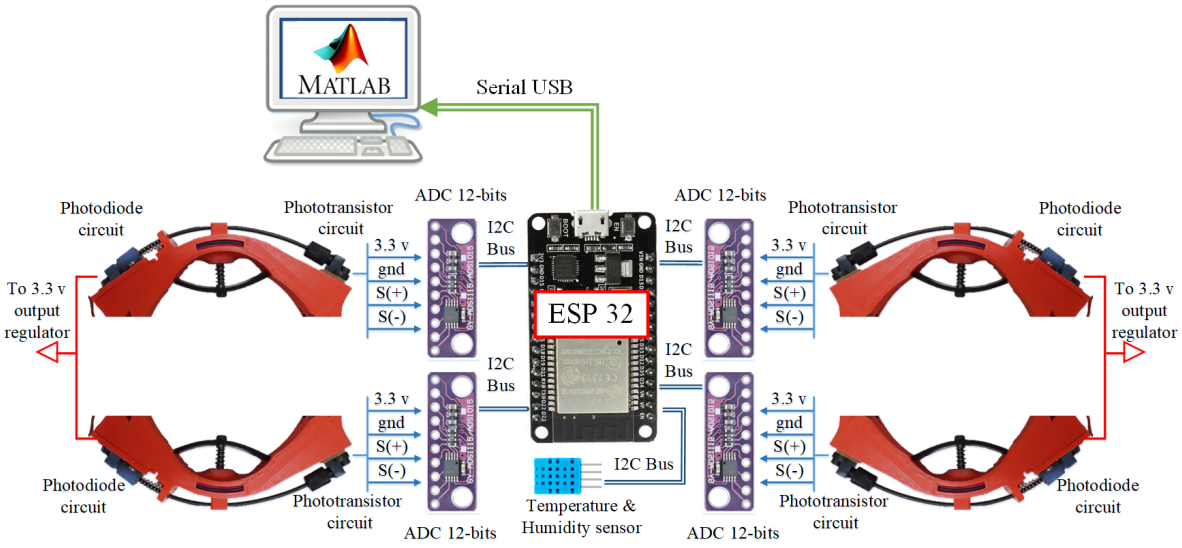

Figure 18 – Electrical circuit diagram of the POF sensor system

3.3 Force Characterization

Figure 19 shows the experimental setup for force characterization of the four POF sensors. The setup was instrumented with a 10 kg-f compression/extension load cell and a signal conditioning circuit (HX711) to provide a force reference.

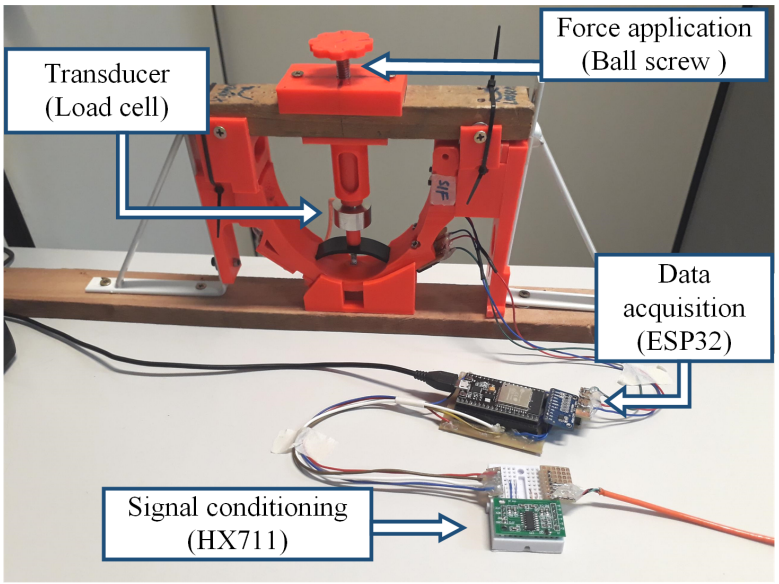

Figure 19 – Experimental setup for force characterization

Compression and release step forces were applied over the diaphragm surface (contact area between human and robot) by rotating a ball screw 360 ° with an approximate stabilization time of 25 minutes. The tests were carried out at an approximately constant temperature and humidity of 29.5 ° and 25% respectively.

Figure 20 presents the results of the characterization of the POF sensors. The first column of plots in this figure displays the time-varying responses of the load cell force

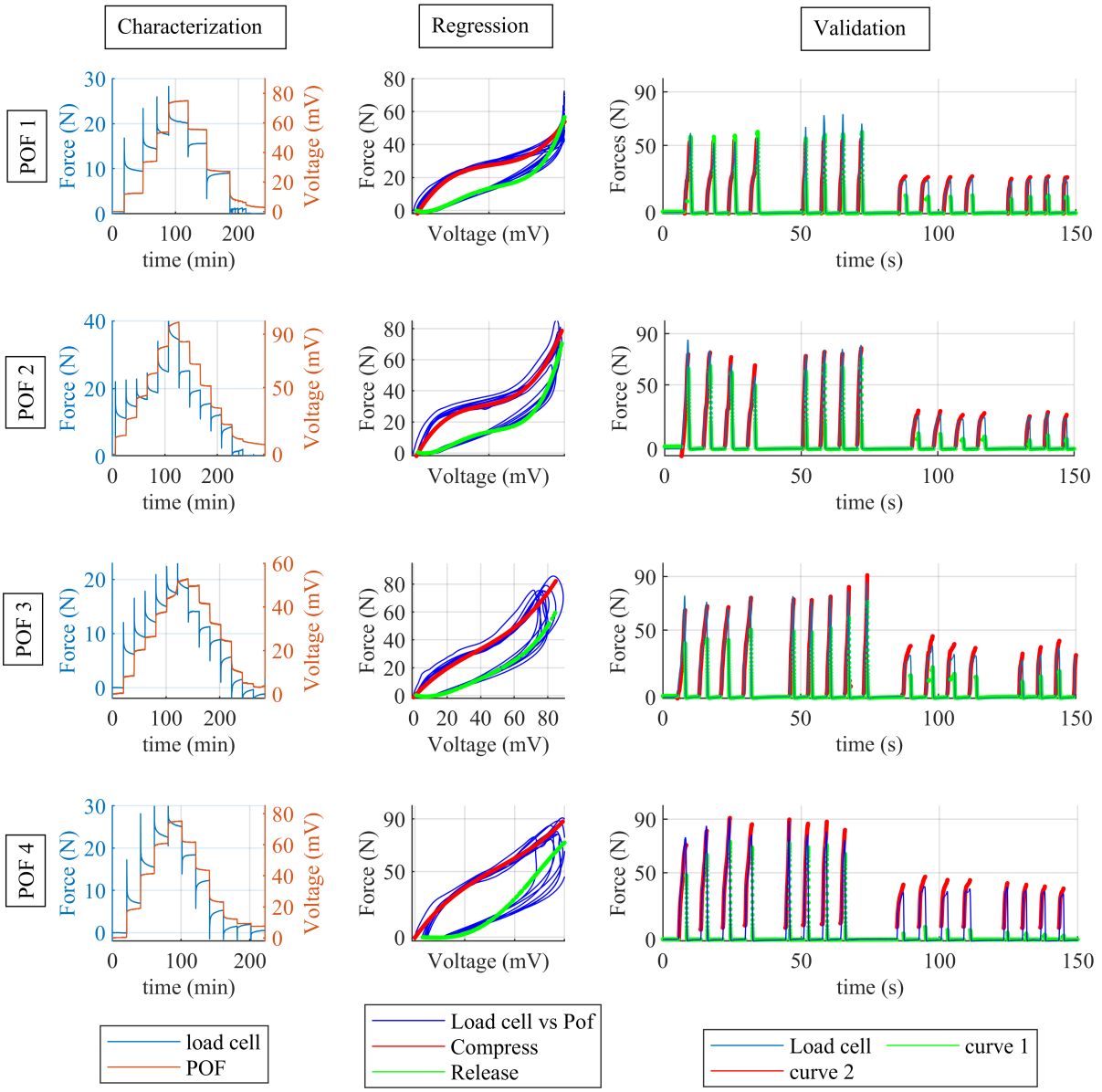

Figure 20 – POF-based sensor force characterization results.

(depicted in blue) and the POF voltage (shown in red) for each POF sensor. These plots provide a direct comparison of the measured forces against the electrical responses of the sensors. The second column of plots further elucidates this relationship by showcasing regression analyses between the load cell force and POF voltage. These plots also highlight the derived polynomial functions representing compression (in red) and release step forces (in green), thereby offering a comprehensive view of the sensor's force-voltage characteristics. The validation of this polynomial regression derived for the POF sensors is illustrated in the third column of plots in Figure 19. A detailed exposition of this validation process, including an analysis of the results, is provided later in Section 3.4.

For POF sensor 1, Equations (3.1) provide polynomial regressions for compression and release step forces, respectively. The high R-square values of 0.9848 and 0.995 obtained

for these forces indicate a strong correlation between the POF sensor readings and the actual forces applied.

$$F_{pof1} = \begin{cases} 1.23e^{-4} \cdot \mathrm{V}_{pof1}^3 - 0.017 \cdot \mathrm{V}_{pof1}^2 + 0.91 \cdot \mathrm{V}_{pof1} - 0.51 & if \frac{\mathrm{d}V_{pof1}}{\mathrm{d}t} > 0 \\ 3.52e^{-6} \cdot \mathrm{V}_{pof1}^4 - 5.36e^{-4} \cdot \mathrm{V}_{pof1}^3 + 0.02 \cdot \mathrm{V}_{pof1}^2 - 0.017 \cdot \mathrm{V}_{pof1} - 0.096 & otherwise \end{cases} \tag{3.1}$$

Similarly, for POF sensors 2, 3, and 4, polynomial regressions, as detailed in Equations (3.2) to (3.4), describe their compression and release step forces. The respective R-square values, notably high for each sensor, affirm the precision and reliability of the sensor responses under varying force conditions. These polynomial functions serve as foundational elements for accurate force assessment within the POF sensor system, contributing significantly to the system's utility in HRI applications.

For POF sensor 2, with R-square values of 0.9728 and 0.9936 for the compression and release step forces, respectively:

$$F_{pof2} = \begin{cases} 1.032e^{-4} \cdot \mathrm{V}_{pof2}^3 - 0.014 \cdot \mathrm{V}_{pof2}^2 + 0.814 \cdot \mathrm{V}_{pof2} + 2.280 & if \frac{\mathrm{d}V_{pof2}}{\mathrm{d}t} > 0 \\ 2.097e^{-7} \cdot \mathrm{V}_{pof2}^4 - 4.65e^{-5} \cdot \mathrm{V}_{pof2}^3 - 0.011 \cdot \mathrm{V}_{pof2}^2 + 0.83 \cdot \mathrm{V}_{pof2} - 6.32 & otherwise \end{cases} \tag{3.2}$$

For POF sensor 3, with R-square values of 0.9779 and 0.9908 for the compression and release step forces respectively:

$$F_{pof3} = \begin{cases} 1.002e^{-4} \cdot \mathrm{V}_{pof3}^3 - 0.012 \cdot \mathrm{V}_{pof3}^2 + 0.729 \cdot \mathrm{V}_{pof3} + 0.329 & if \frac{\mathrm{d}V_{pof3}}{\mathrm{d}t} > 0 \\ 1.95e^{-6} \cdot \mathrm{V}_{pof3}^4 - 2.086e^{-4} \cdot \mathrm{V}_{pof3}^3 + 0.007 \cdot \mathrm{V}_{pof3}^2 - 0.22 \cdot \mathrm{V}_{pof3} - 2.13 & otherwise \end{cases} \tag{3.3}$$

For POF sensor 4, with R-square values of 0.9877 and 0.9374 for the compression and release step forces, respectively:

$$F_{pof4} = \begin{cases} 3.03e^{-5} \cdot \mathrm{V}_{pof4}^3 - 0.007 \cdot \mathrm{V}_{pof4}^2 + 1.067 \cdot \mathrm{V}_{pof4} - 0.389 & if \frac{\mathrm{d}V_{pof4}}{\mathrm{d}t} > 0 \\ -3.2e^{-7} cdot \mathrm{V}_{pof4}^4 + 8.56e^{-5} \cdot \mathrm{V}_{pof4}^3 - 0.002 \cdot \mathrm{V}_{pof4}^2 - 0.003 \cdot \mathrm{V}_{pof4} + 0.023 & otherwise \end{cases} \tag{3.4}$$

3.4 Validation of POF sensors

The POF sensors were validated by manually applying repetitive impulse forces. Each force was exerted for approximately 2 seconds, followed by a 4-second gap before the next application. This method was chosen to mimic the dynamic forces typically encountered in human-robot interaction scenarios. During the validation experiments, the time derivative of the POF signal voltages was computed to differentiate between the

compression and release phases. This precise detection of force transitions was crucial for understanding the sensor's performance.

The positive rate of voltage change indicated the application of a compression force, while a negative rate of voltage change indicated the application of a release force. This distinction is important to understand the sensor response under varying force conditions. The validation results, displayed in the third column of plots in Figure 20, demonstrate the sensor's performance under both compression and release forces. Furthermore, Table 4 presents the performance metrics for each POF sensor's regression curves, validating the sensor's efficiency in capturing the forces involved in HRI systems.

	RMSE (Newton)	
	Curve 1 (compression)	Curve 2 (release)
POF 1	0.8559	0.4318
POF 2	1.45	0.7158
POF 3	0.9339	0.5431
POF 4	3.252	3.144

Table 4 – Performance metrics of the POF sensors for force assessment.

3.5 Experimental Results

This section presents the experimental results obtained using the proposed POF-based sensor associated with the exoskeleton Exo-TAO. As shown in Figure 21, a voluntary user was asked to wear the exoskeleton Exo-TAO with the knee actuator coupled to it and walk on a treadmill at his own preferred comfortable walking speed. Meanwhile, the DOB-based estimation techniques were implemented.

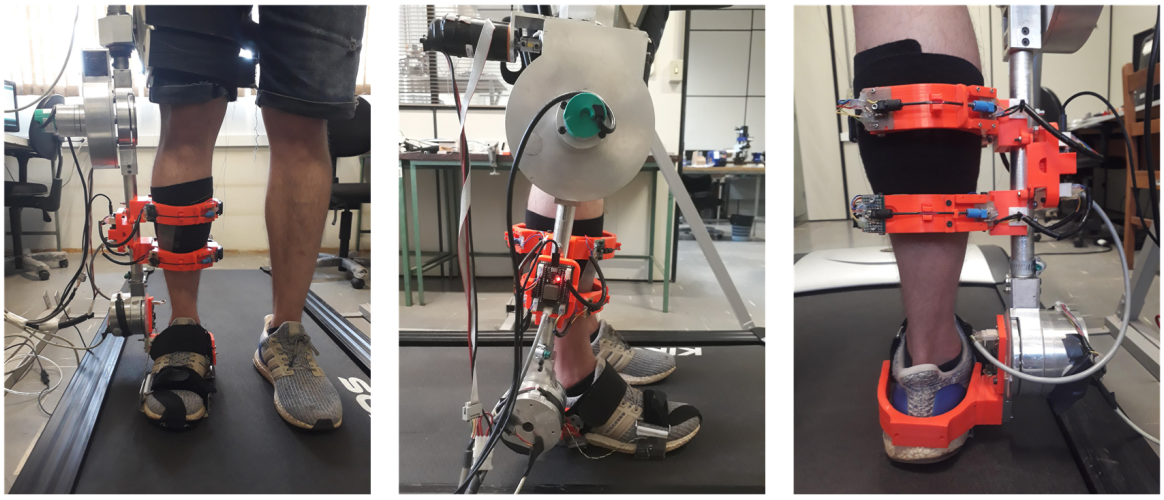

Figure 21 – Experimental setup of POF sensor.

The interaction torque can be approximated to the provided by the POF sensor, i.e., τ_{POF} which considers the four force measurements and the position of each sensor, as

shown below:

$$\tau_{int} \approx \tau_{POF} = l_1 * (F_{pof1} + F_{pof3}) + l_2 * (F_{pof2} + F_{pof4}). \tag{3.5}$$

Figure 22 shows the estimation results. The upper plot shows the estimation results of the techniques that consider ideal alignment, and the bottom plot shows the estimation results of the techniques that consider misalignment in the model.

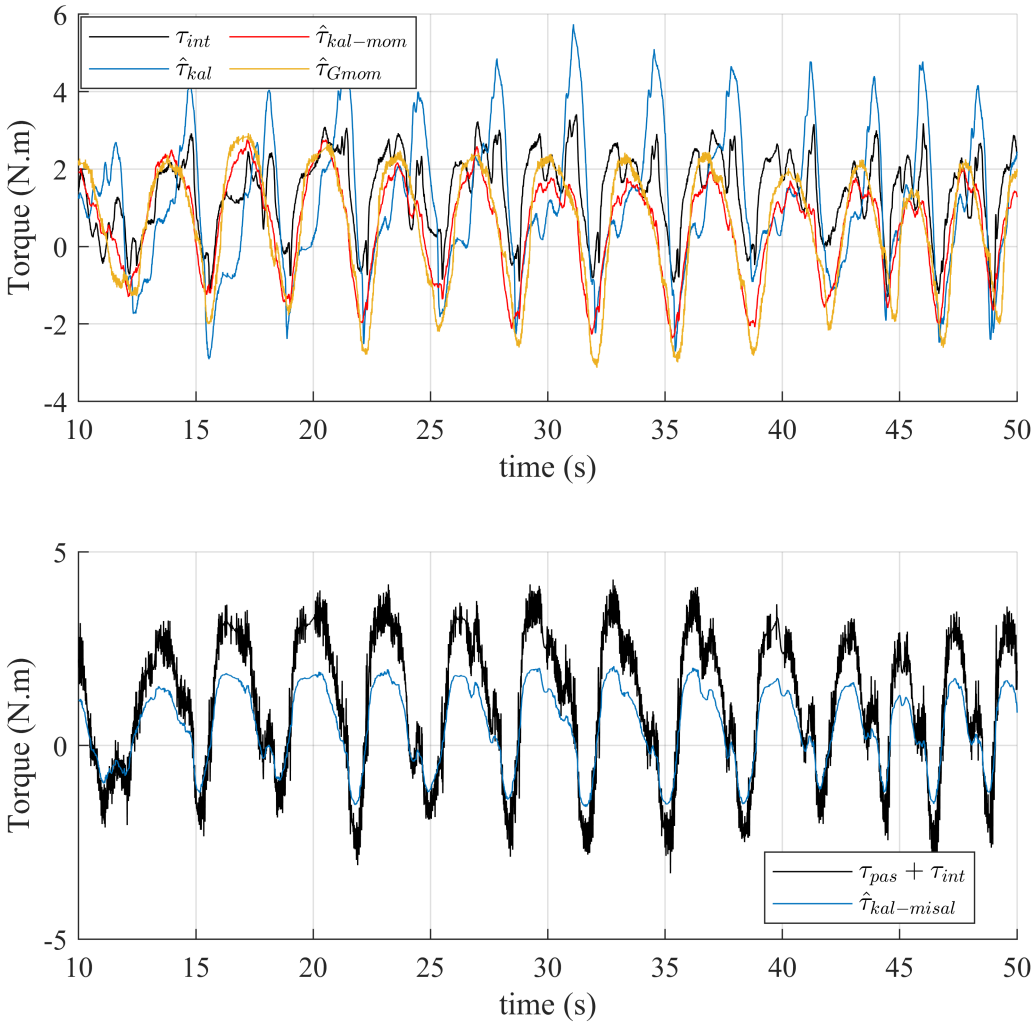

Figure 22 – Estimated interaction and human torque using the POF-based sensor.

Table 5 shows the values of Root Mean Square Error (RMSE), Dynamic Time Warping index (DTW), and Time Lag (Lag) using cross-correlation for the estimated interaction torques, considering as the ground true the interaction torque given by the POF-sensor, τ_{POF}, for the estimated interaction torques, and the human torque given by the POF-sensor, $\tau_{h_{POF}}$, for the estimated human torque, $\hat{\tau}_{h_{Kal\_misal}}$.

Index	$\hat{\tau}_{Kal}$	$\hat{\tau}_{Kal\_Gmom}$	$\hat{\tau}_{Gmom}$	$\hat{\tau}_{Kal\_misal}$
RMSE	1.0518	1.2184	1.4241	0.2199
DTW	94.4715	85.6758	111.7527	27.4129
Time Lag	-0.2669	-0.3203	-0.3523	0.0107

Table 5 – Performance indexes for torque estimation using the POF sensor.

4 FSR-BASED HRI SENSOR WITH DIFFERENTIAL MEASUREMENTS

This study introduces an innovative approach to assessing interaction forces in human-robot interfaces using Force-Sensing Resistor (FSR) sensors, similar to the POF-based sensor.

4.1 Sensor Assembly

Figure 23a illustrates the assembly of an FSR sensor module. Each module has an FSR sensor (Tekscan Standard Model ESS102) embedded in a 3D-printed structure shaped to the leg's curvature. The sensor positions are chosen to capture interaction forces at four distinct points on the shank: two at the front and two at the back. The modules are integrated at the interfaces between the leg and the robot cuffs, ensuring precise detection of contact point forces. The FSR sensor specifications include a force range of 0-4N, a length of 38.1 mm, and a sensing diameter of 3.81 mm, enabling precise detection of contact point forces at the interface. Comfort and safety are also considered, with layers of silicone rubber and polyurethane foam included at each FSR module to prevent skin damage.

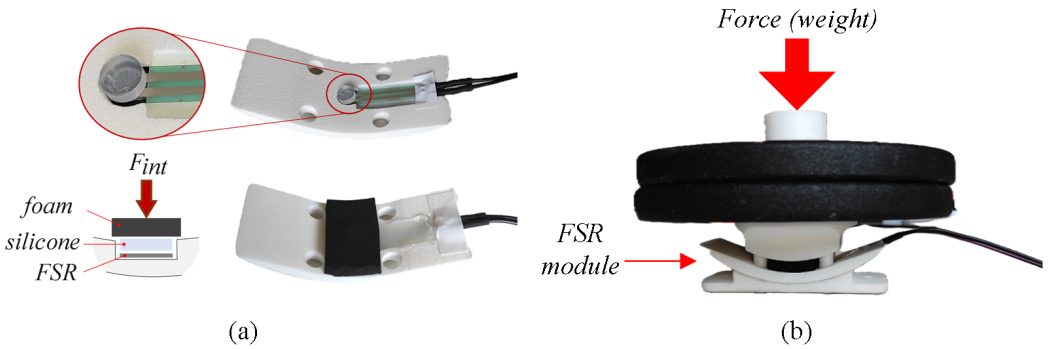

Figure 23 – FSR sensor module.
(a) Assembly (b) Setup for force characterization

4.2 Force Characterization

The experimental setup for characterizing the four FSR sensor modules is displayed in Figure 23b. The characterization process involved applying known fixed-weight loads incrementally every 5 minutes, allowing the sensors to experience both compression and release forces.

Data were collected using LabVIEW, and polynomial regression functions were computed to model the sensor responses. Figure 24 depicts the time responses of the inputs and output signals during these experiments. A simple validation involving repetitive

application of a single weight for compression and release at 5-minute intervals yielded high accuracies, as evidenced by the computed R-squared values in Figure 24.

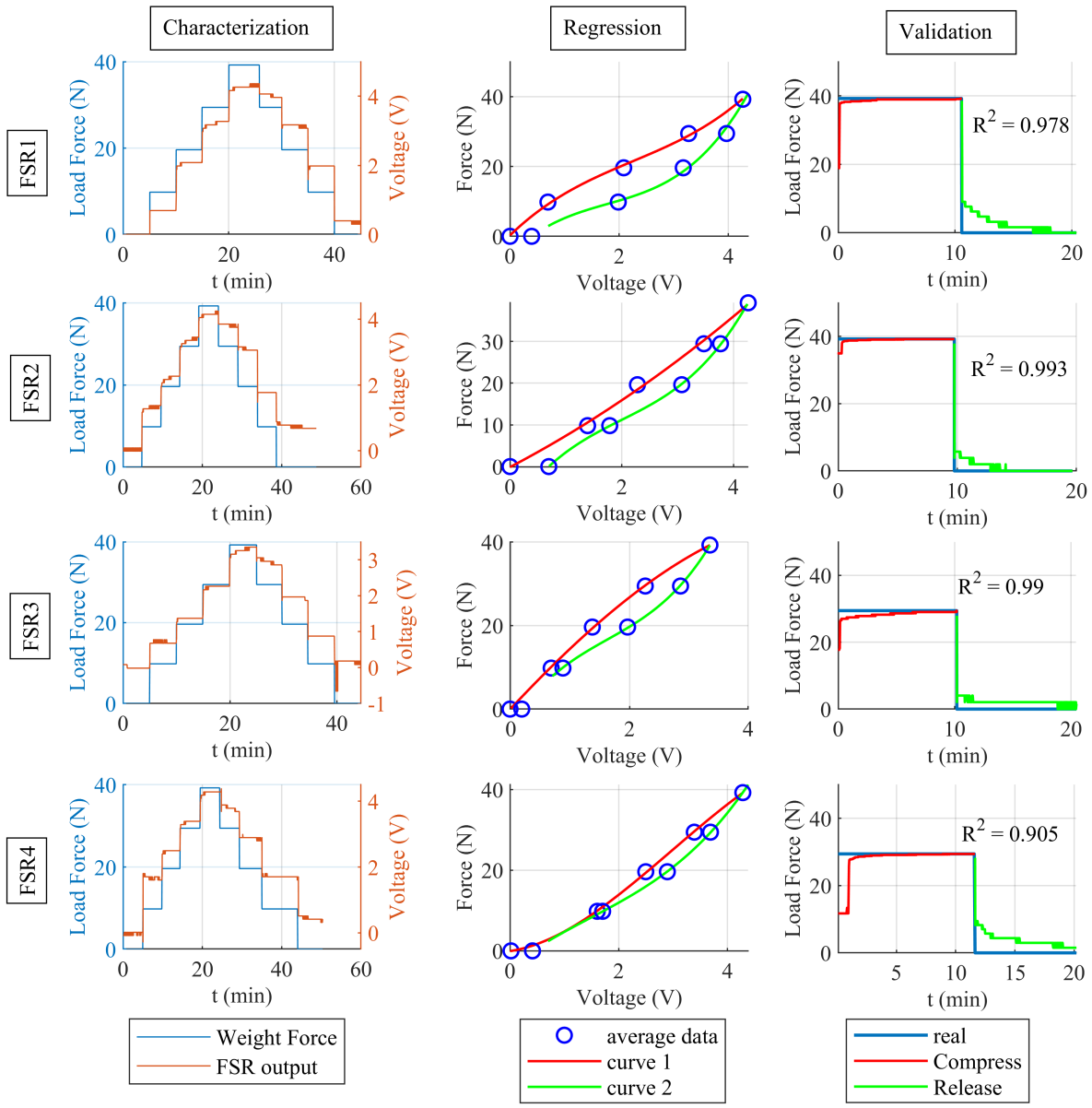

Figure 24 – Time responses of force characterization experiments

The force measurements were modeled using third-order polynomial functions for compression forces and fourth-order polynomial functions for release forces, as described in the following equations for each FSR sensor module.

$$F_{fsr1} = \begin{cases} 0.566 \cdot \mathrm{V}_{fsr1}^3 - 3.815 \cdot \mathrm{V}_{fsr1}^2 + 15.144 \cdot \mathrm{V}_{fsr1} + 0.289 & if \frac{\mathrm{d}V_{fsr1}}{\mathrm{d}t} > 0 \\ 1.173 \cdot \mathrm{V}_{fsr1}^3 - 6.278 \cdot \mathrm{V}_{fsr1}^2 + 15.649 \cdot \mathrm{V}_{fsr1} - 5.341 & otherwise \end{cases} \tag{4.1}$$

$$F_{fsr2} = \begin{cases} 0.004 \cdot \mathrm{V}_{fsr2}^3 + 0.485 \cdot \mathrm{V}_{fsr2}^2 + 7.014 \cdot \mathrm{V}_{fsr2} - 0.119 & if \frac{\mathrm{d}V_{fsr2}}{\mathrm{d}t} > 0 \\ 1.109 \cdot \mathrm{V}_{fsr2}^3 - 6.635 \cdot \mathrm{V}_{fsr2}^2 + 19.932 \cdot \mathrm{V}_{fsr2} - 10.996 & otherwise \end{cases} \tag{4.2}$$

$$F_{fsr3} = \begin{cases} -0.083 \cdot \mathrm{V}_{fsr3}^3 - 0.773 \cdot \mathrm{V}_{fsr3}^2 + 15.161 \cdot \mathrm{V}_{fsr3} + 0.183 & if \frac{\mathrm{dV}_{fsr3}}{\mathrm{dt}} > 0 \\ 1.703 \cdot \mathrm{V}_{fsr3}^3 - 8.332 \cdot \mathrm{V}_{fsr3}^2 + 21.554 \cdot \mathrm{V}_{fsr3} - 3.693 & otherwise \end{cases} \quad (4.3)$$

$$F_{fsr4} = \begin{cases} -0.356 \cdot \mathrm{V}_{fsr4}^3 + 3.192 \cdot \mathrm{V}_{fsr4}^2 + 2.026 \cdot \mathrm{V}_{fsr4} - 0.053 & if \frac{\mathrm{dV}_{fsr4}}{\mathrm{dt}} > 0 \\ 0.500 \cdot \mathrm{V}_{fsr4}^3 - 2.203 \cdot \mathrm{V}_{fsr4}^2 + 10.352 \cdot \mathrm{V}_{fsr4} - 3.933 & otherwise \end{cases} \quad (4.4)$$

4.3 Misalignment Assessment in a Walking Scenario

The assessment of the misalignment using the FSR sensors in a series of eight experiments to examine the interplay between walking speed, misalignment, and type of interaction. To this, the sensors were tested in a walking robotic rehabilitation scenario by using the EICoSI knee exoskeleton (Rifai *et al.*, 2017) (Figure 14). Four Inertial Measurement Unit (IMU) Wireless Systems from Xsens were used to compute the human knee angle and capture the orientation angles of the shank and thigh segments, both for the human and the robot, as shown in Fig. 25.

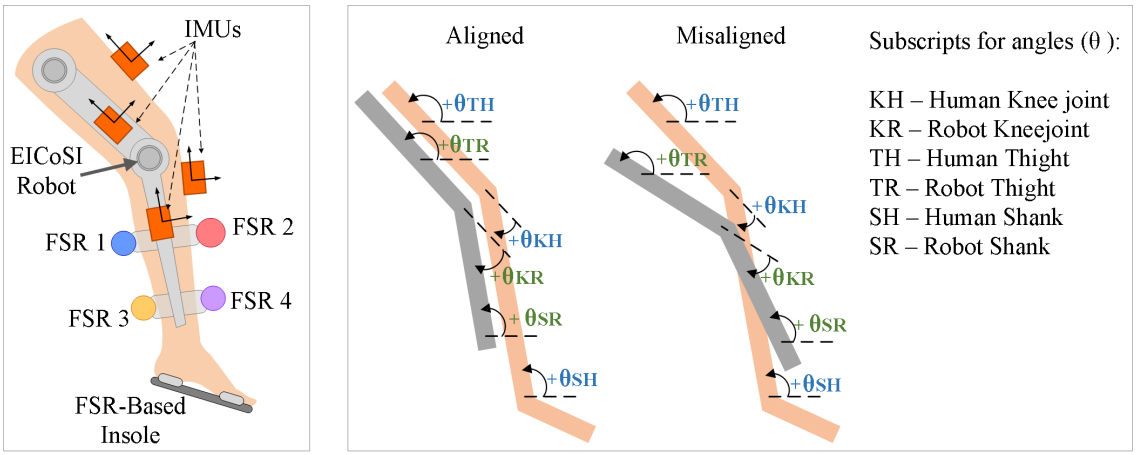

Figure 25 – Experimental Setup for misalignment assessment using the EICoSI (a) sensor positioning (b) angles measured by the IMU sensors

two placements of the robot knee joint was tested to adding different alignments in the experiments: firstly, the device was worn to the user in the best possible aligned to the leg, and sufficiently tightened, ensuring minimal shear forces and slippage; secondly, the device was shifted 10 cm downwards from the knee's normal position distal joint to introduce a misalignment between the human and the robot.

Regarding the types of interaction behavior tested, the control mode of the robot was tested in two scenarios: a zero impedance control (No Assistance) and trajectory control with predefined reference trajectories. In the latter, the robot's impedance control was programmed to track predefined reference trajectories with a virtual stiffness gain of

$K_v = 60Nm/rad$. These trajectories were estimated previously by asking the volunteer to walk on a treadmill without the exoskeleton at speeds of 1 m/s and 2 m/s. Subsequently, using IMU sensors, the knee joint angle was computed and recorded at these two speeds and then segmented to create a mean signal describing the knee joint angle trajectory during the gait cycle for both velocities. Finally, an FSR-based insole was employed to detect the two main phases during gait, namely the stance and swing phases. Details of these experiments are provided in Table 6.

Exp. Number	Robot Position	Control Mode	Walking Speed (m/s)
1	Aligned	No Assistance	1
2	Aligned	No Assistance	2
3	Aligned	Trajectory Assistance	1
4	Aligned	Trajectory Assistance	2
5	Misaligned	No Assistance	1
6	Misaligned	No Assistance	2
7	Misaligned	Trajectory Assistance	1
8	Misaligned	Trajectory Assistance	2

Table 6 – Experiments with the EICoSI and the FSR sensors.

4.4 Experimental Results

Figure 28 presents the FSR signals obtained from the experiments conducted under aligned and misaligned conditions. The signals from each experiment were segmented across the gait cycle, and the mean value of these segmented signals was calculated. In the plots, each signal is represented according to the sensor's response computed using the corresponding polynomial function, with shadow regions representing the standard deviation of each signal. As expected, there are considerable differences in amplitude levels between the aligned and misaligned cases. The misaligned experiments exhibit higher amplitude signals, consistent with the expectation that misalignment leads to increased pressures and higher interaction forces at the sensor interface.

Overall, all FSR sensors exhibited changes in amplitude levels when subjected to the misalignment conditions. However, it was observed that the sensors located at distal points to the knee joint, specifically FSR2 and FSR4, demonstrated a lower sensitivity to variations in their dynamic response. In contrast, the signals from FSR1 and FSR3, positioned closer to the knee joint, exhibited amplified peak regions due to the effect of misalignment. This resulted in distinct patterns in their dynamic response, reflecting the direct impact of misalignment on these sensors. The signals from the front shank sensors (FSR2 and FSR4), which are situated closer to the bone, yielded a more consistent pattern than the rear sensors (FSR1 and FSR3) in contact with the gastrocnemius muscle. The

greater variations in the signals of the rear sensors highlight the differential impact of forces on various regions of the shank. Such observations underscore the importance of sensor placement in accurately capturing the nuances of human-robot interaction forces.

These signals were normalized, bypassing any analysis of their magnitudes or RSM values and focusing on the time effects of the misalignment. In these plots, the continuous signals represent the normalized mean values, while the triangle symbols represent the characteristic peaks of each signal. The dashed lines in all plots delineate the boundaries of the two primary phases of walking, with the stance phase preceding the swing phase.

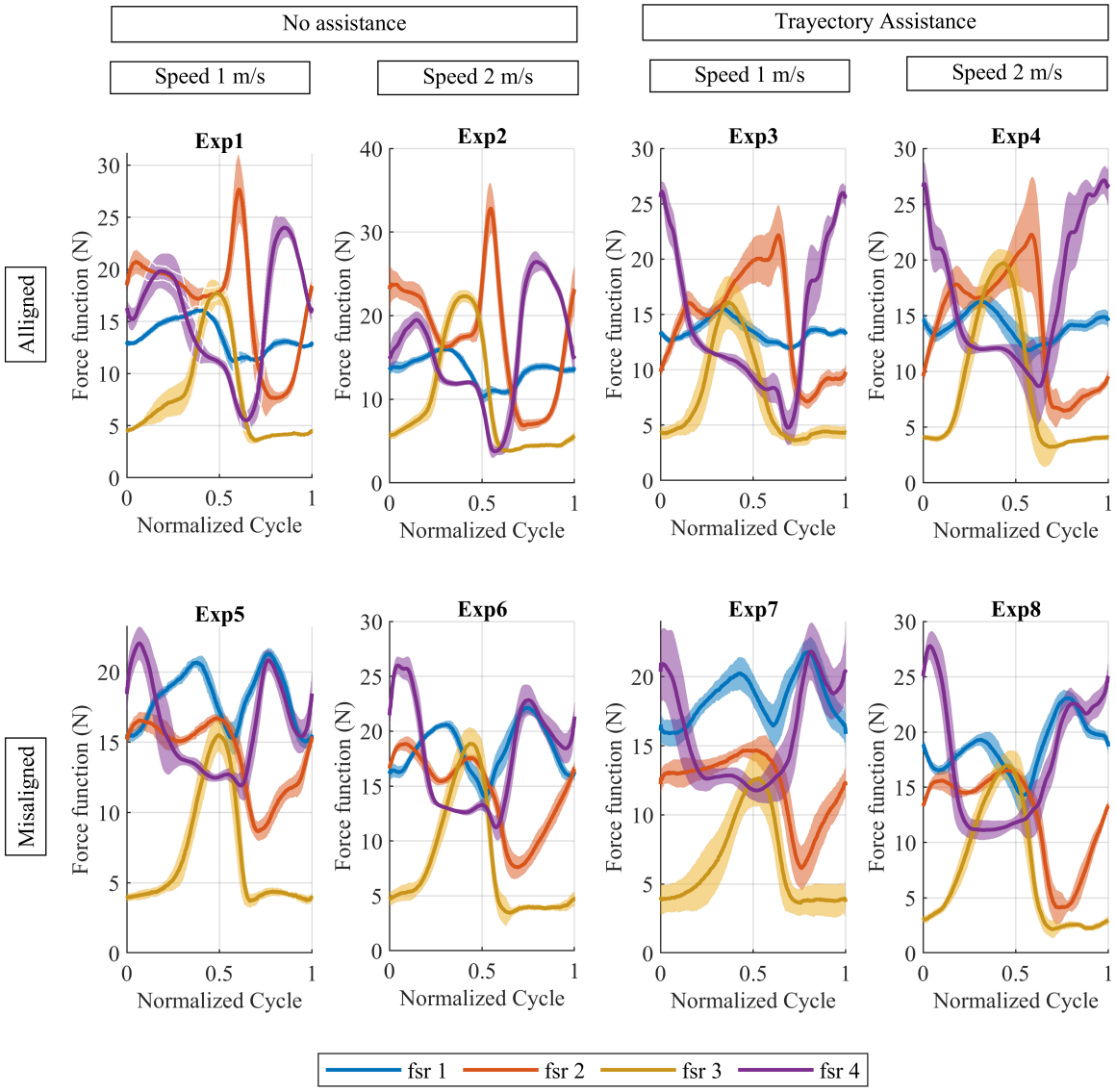

Figure 26 – FSR signals over the gait cycle for the experiments with 1 m/s.

Table 7 shows the occurrence of Peaks in the FSR signals during the normalized time. The table was calculated to observe timing differences between the different types of experiments. In the table, gray cells indicate which experiment between aligned or misaligned performed earlier occurrence.

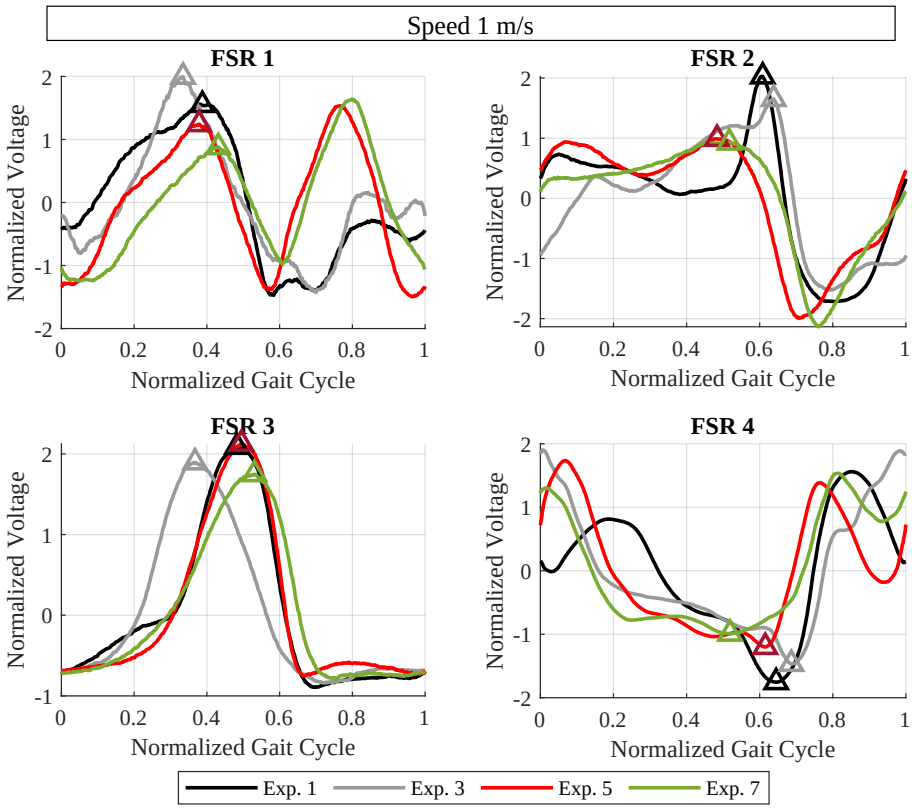

Figure 27 – FSR signals over the gait cycle for the experiments with 2 m/s.

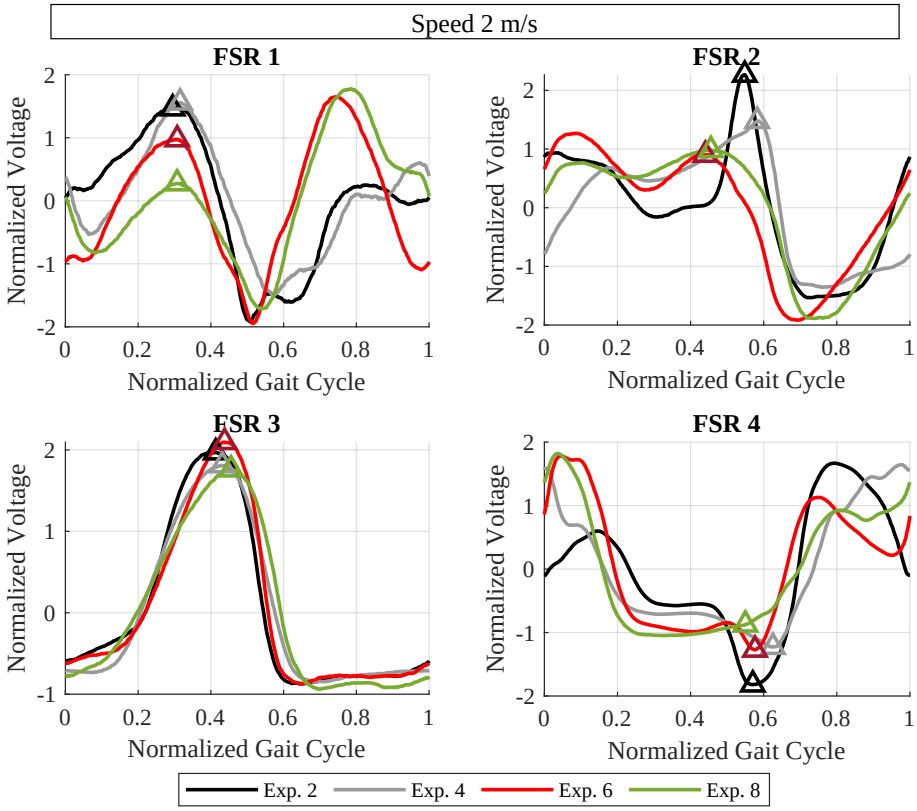

Figure 28 – FSR signals over the gait cycle for the experiments.

	Walking speed 1 m/s				Walking speed 2 m/s			
	No Assistance		Trayectory Assistance		No Assistance		Trayectory Assistance	
	Alig (Exp1)	Misalig (Exp5)	Align (Exp3)	Misalig (Exp7)	Align (Exp2)	Misalig (Exp6)	Align (Exp4)	Misalig (Exp8)
FSR 1	0.3874	0.3787	0.3346	0.4314	0.2948	0.3075	0.3154	0.3073
FSR 2	0.6082	0.4832	0.6383	0.5169	0.5482	0.4404	0.5822	0.4555
FSR 3	0.4827	0.4951	0.3675	0.5308	0.4132	0.4377	0.4313	0.4555
FSR 4	0.6450	0.6154	0.6867	0.5189	0.5702	0.5762	0.6253	0.5499

Table 7 – Peak occurrences in a normalized cycle of experiments

The mean ratios and differences of the knee joint (θ_K), thigh (θ_T), and shank (θ_S) angles between the human and the robot are computed and displayed as a bar plot in Fig. 29. Here, the angle differences are denoted by (Δ) and the ratio by R. The mean angle differences are expressed in radians, while the ratio is dimensionless. Fig. 30 presents all experiments' average cycle duration in percentages for the gait phases. The stance phase for experiments with aligned and misaligned configurations is represented by blue and light blue colors, respectively. Similarly, the swing phase for experiments with aligned and misaligned configurations is denoted by red and salmon colors, respectively. A hatched fill pattern distinguishes experiments with trajectory assistance.

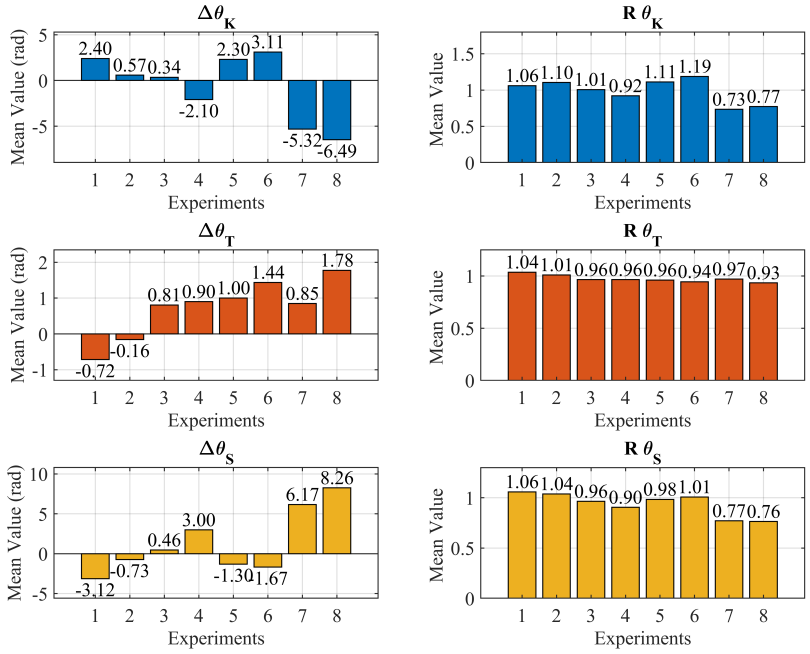

Figure 29 – Bar plot of the mean angle ratios and differences.
(Δ for difference and R for ratio) between the human and robot for knee joint (θ_K), thigh (θ_T), and shank (θ_S) angles.

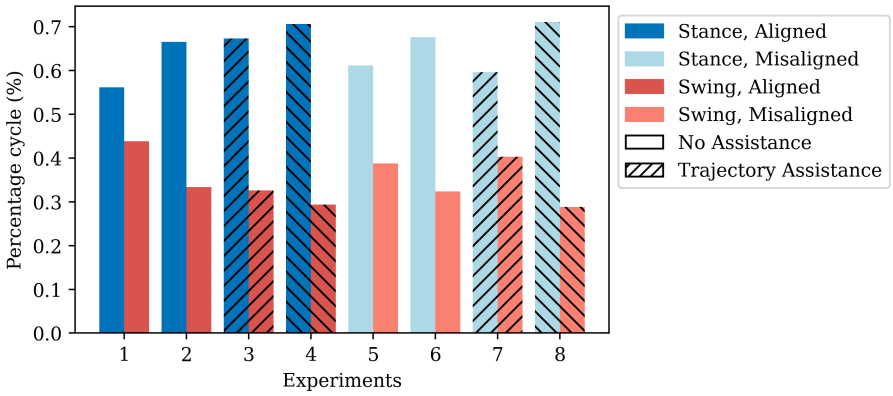

Figure 30 – Average cycle duration percentages for the gait phases across all experiments.

4.4.1 Torque estimation results

This section shows the outcomes of employing the FSR-based HRI sensor to estimate human joint torque using DO techniques. To assess the results of the techniques, an experiment was carried out with a volunteer, following the specifications detailed in experiment number 5, as listed in Table 6. Figure 31 shows the times responses of the estimated torques.

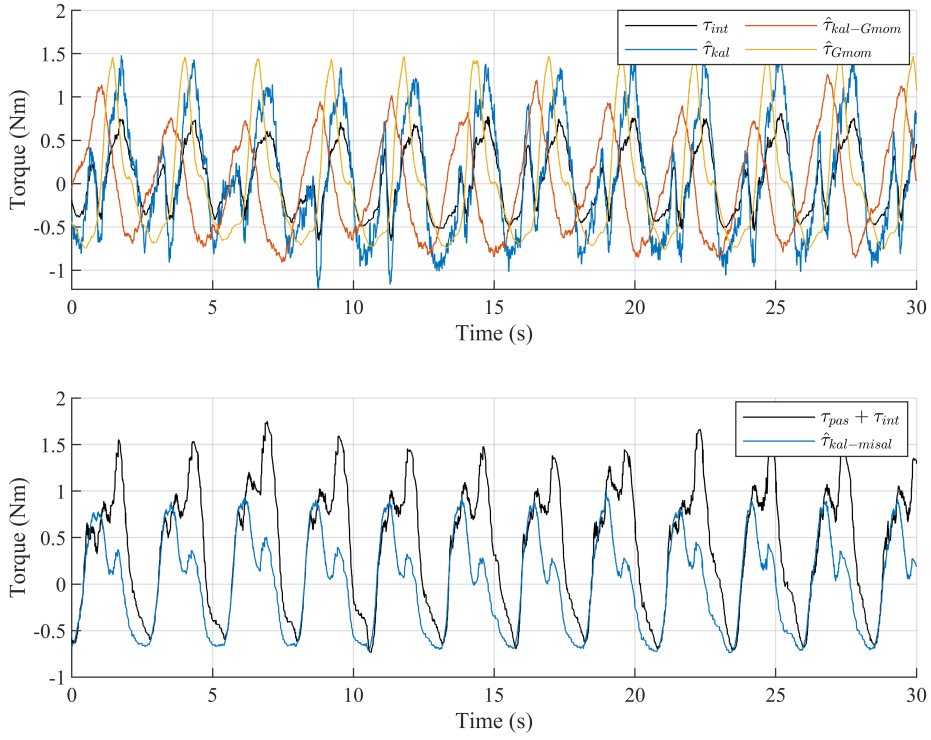

Figure 31 – Estimated interaction and human torque using the FSR sensor.

Table 8 shows the values of Root Mean Square Error (RMSE), Dynamic Time Warping index (DTW), and Time Lag (Lag) using cross-correlation for the estimated

interaction torques, considering as reference the interaction torque, τ_{int} , computed from the FSR lectures.

Index	$\hat{\tau}_{Kal}$	$\hat{\tau}_{Kal\_Gmom}$	$\hat{\tau}_{Gmom}$	$\hat{\tau}_{Kal\_misal}$
RMSE	0.1488	1.3002	0.8601	0.6189
DTW	29.4025	223.8465	139.2251	145.2586
Time Lag	0.0150	0.7950	0.2950	0.0950

Table 8 – Performance indexes for torque estimation using the FSR sensor.

5 FSR SENSOR ARRAY FOR HRI AND MISALIGNMENT ASSESSMENT

This chapter introduces developing, characterizing, and evaluating an innovative approach using a FSR sensor array. This array is designed to provide a comprehensive coverage of interaction forces, advancing beyond the four-point interaction approach utilized in previous sensor systems. A key innovation of this prototype is its enhanced capability to describe the HRI forces at the cuff interfaces accurately.

5.1 Interaction Mapping with the FSR Sensor Array

In an ideal human-robot system, there is no misalignment, and the leg and robot link movements are perfectly synchronized. Under such conditions, strategically positioning force measurement zones at two points — one at the front and the other at the back of the leg — would suffice to capture all interaction forces in the sagittal plane (Figure 32a). However, in the presence of misalignment, this assumption fails. The leg and robot links are desynchronized, leading to skin shearing, movement of attachments, and unpredictable parasitic forces and torques.

Compliance features are often incorporated in braces and cuffs to mitigate these undesired effects, reducing hardness and shear forces. While this approach minimizes misalignment impacts, it also allows rotation along the leg's longitudinal axis. Such rotation influences force detection in the sagittal plane, as the sensors, being attached to the robot, rotate with misalignment, altering the magnitude of detected HRI forces (Figure 32b).

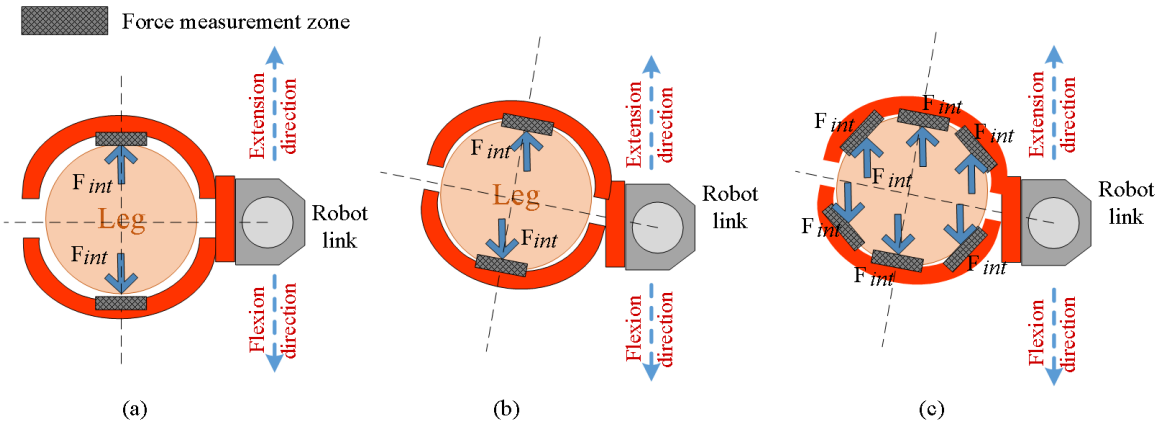

Figure 32 – Conceptual diagrams of interaction point measurement.
(a) Ideal Alignment (b) Misalignment Impact (c) Misalignment with Multiple Interaction Points

This chapter proposes a sensor prototype that includes multiple interaction point measurements to comprehensively map the dynamics of misalignment, addressing the

effects of rotations and shear forces at the interface (Figure 32c).

5.2 Sensor Assembly

Figure 33a illustrates the assembly of the proposed sensor prototype. Constructed using 3D printing with ABS filament, it incorporates two hinge joints for adaptable positioning on different leg anthropometries. Similar to the FSR sensor system discussed in Section 4.1, this prototype emphasizes comfort and safety, incorporating silicone rubber and polyurethane foam at each sensor contact point.

The sensor system is designed to detect interaction forces at four zones around the leg. Unlike previous prototypes, the front contact zones consist of three FSR sensors arranged 45 degrees apart within the internal structure. The FSR sensor array comprises eight sensors numerically labeled from 1 to 8. The distribution of these sensors within the prototype is depicted in Figure 33b.

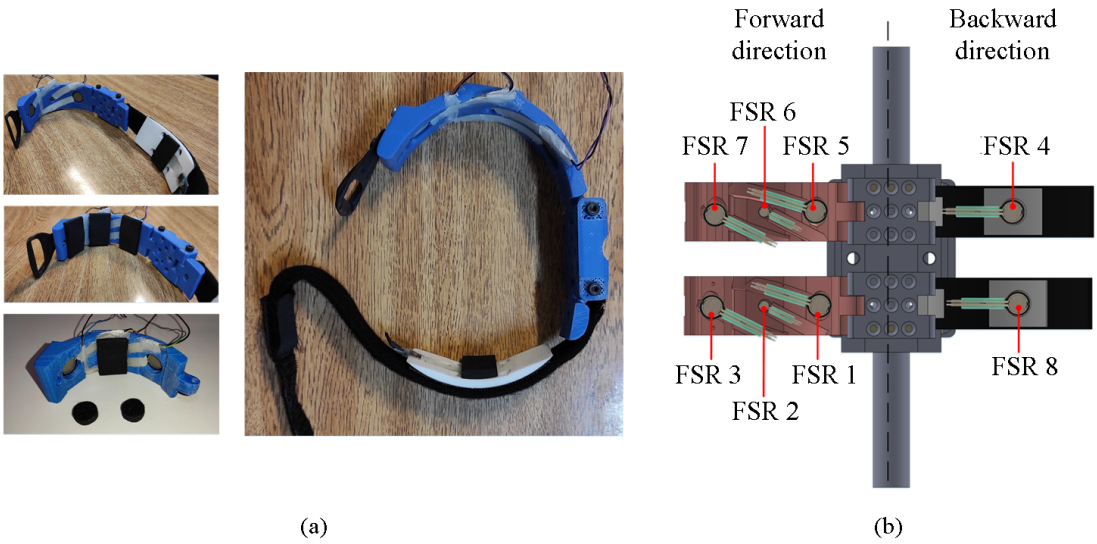

Figure 33 – FSR Sensor Array
(a) Detailed Assembly (b) Sensor Distribution

5.3 HRI force characterization

This section outlines the experimental setup devised for characterizing the FSR sensor array. The eight FSR signals from the array were compared with a six-axis Force/Torque (F/T) transducer to assess interaction forces and the effects of misalignment. The six-axis Force/Torque transducer (ATI Industrial Automation AXIA80–M20) was used to measure interaction forces and torques in all three Cartesian coordinates (x, y, and z). It was placed between the robot link of the Rotary SEA setup and the FSR sensor array to capture comprehensive interaction force data (see Figure 34).

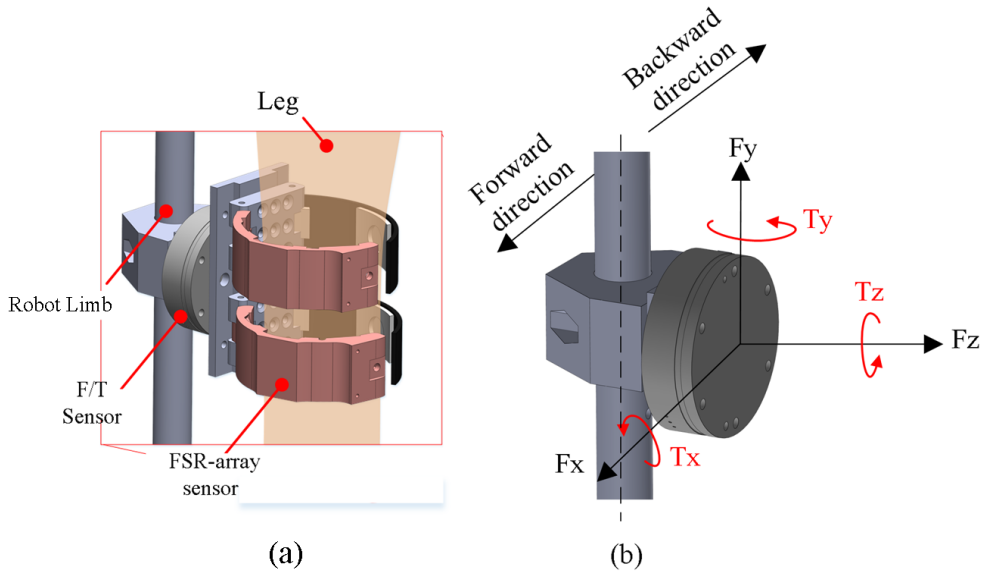

Figure 34 – Setup for HRI force characterization using the FSR Sensor Array system (a) Assembly (b) Coordinate system of F/T sensor

The complexity of the dataset encompasses a diverse set of information on the type of interactions, alignment, and users. Each FSR module in the array influences the interaction force that happens during experiments. Unlike the above sensors, The force characterization is not computed by adding up the total force detected by each FSR sensor module. Instead of this, it is considered which FSR sensors have a stronger influence for predicting the interaction force depending on the changes in each experiment of type interaction, misalignment, and user anthropometry. This section presents the development of a force characterization based on neural networks for regression.

Given that F_x and T_z operate on the sagittal plane, they encapsulate the bulk of the interaction torque dynamics observed throughout the experiments. Figure 35 shows the incidence of these torques on the human leg, while Figure 36 highlights the equivalence between the force F_x, when multiplied by its respective lever arm, and the torque τ_z. Consequently, this section focuses on the regression analysis of the variables F_x and T_z.

5.3.1 Design of Neural Networks for Regression Analysis

Backpropagation neural networks were designed to predict F_x and τ_z. The regression of the other F/T variables follows the same design and similar methodology. Preliminary data analysis, including Neighborhood Component Analysis (NCA), was conducted to identify the most influential FSR inputs for each F/T variable. The NCA results guided the selection of input features for the networks. For instance, the network for predicting the F_x component of force considered inputs primarily from FSR 6, FSR 4, FSR 2, and FSR 8, as these were identified as the most influential for this variable. The torque component Tz is affected by the inputs from FSR 4, FSR 6, FSR 8, and FSR 2. Similarly, inputs for

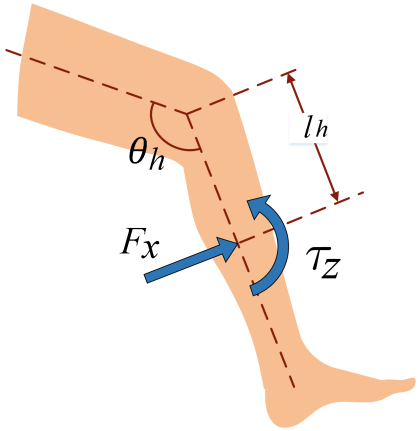

Figure 35 – Comparison between Fx and Tz to represent the interaction torque.

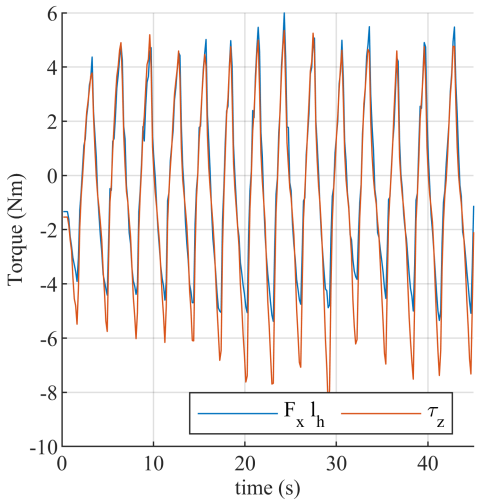

Figure 36 – Time responses of Fx and Tz.

other F/T variables were selected based on their respective NCA feature importance.

Hence, dimensionality reduction can be done to maximize prediction accuracy without a high computational cost. Figure 37 shows the NCA for the dataset arrangments. The NCA was computed twice by grouping the dataset by type of interaction and misalignment. The dataset was analyzed by observing the influence of the feature weights on the type of alignment and experiments.

Given the resemblance in weight patterns between the two NCA analyses, the common features with the most important weights for both NCA analyses were found. Figure 38 shows the selection of these features. This integration offers a comprehensive perspective on the influential factors across these different scenarios. The dimensionality reduction allowed the design of more efficient models for the regression of the six variables of the F/T sensor. Figure 39 illustrates the diagram for implementing the net used for the regression of F_x.

5.3.2 Network Training and Validation

Once it is known which FSR variables have the most importance in predicting F_x and T_z, the selection of the network parameters is conducted by a combination of empirical testing. The architecture comprised two hidden layers, each consisting of four neurons. This configuration was selected to balance the network's complexity and its ability to model the relationships between inputs and the target variable effectively. The networks were trained using a dataset comprising various experiments, alignments, and user interactions. A portion of the data was reserved for validation purposes.

To evaluate the regression of Fx and Tz under aligned and misaligned conditions, two different tests were carried out with one of the dataset group's voluntary users. The first experiment was set with an interaction type 1 and the aligned configuration. The

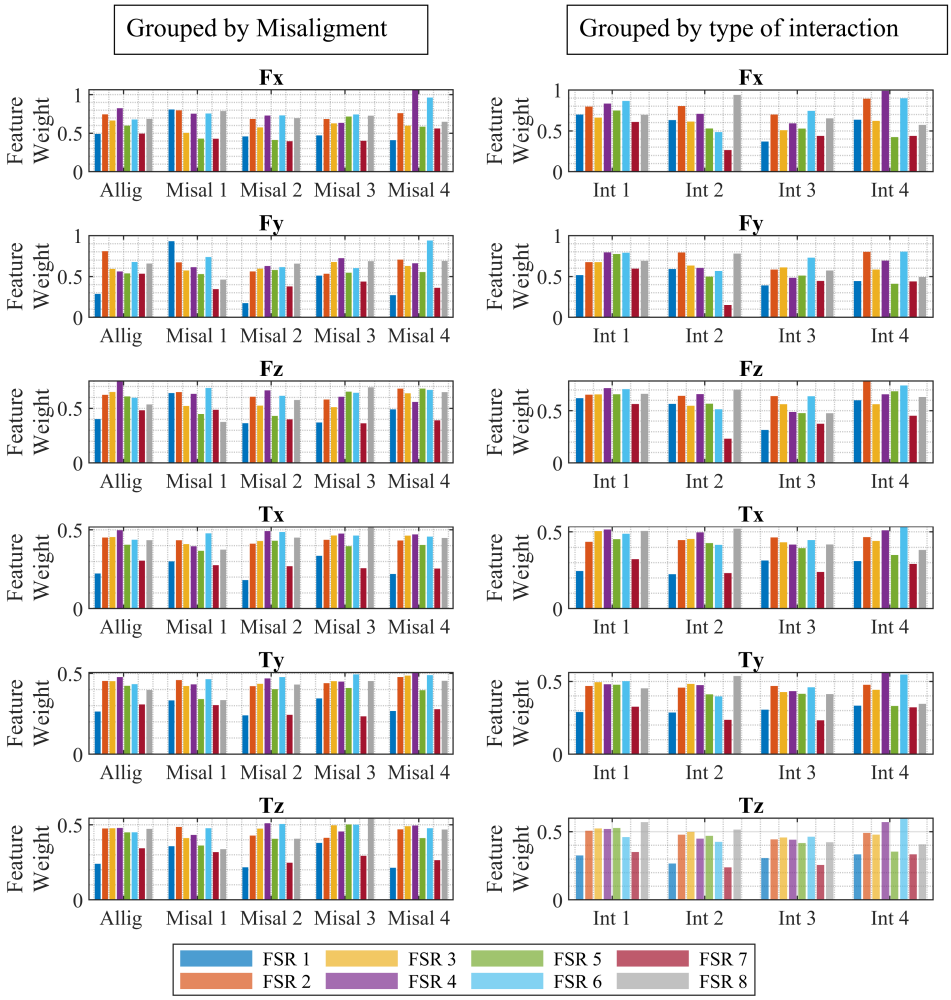

Figure 37 – NCA feature selection.

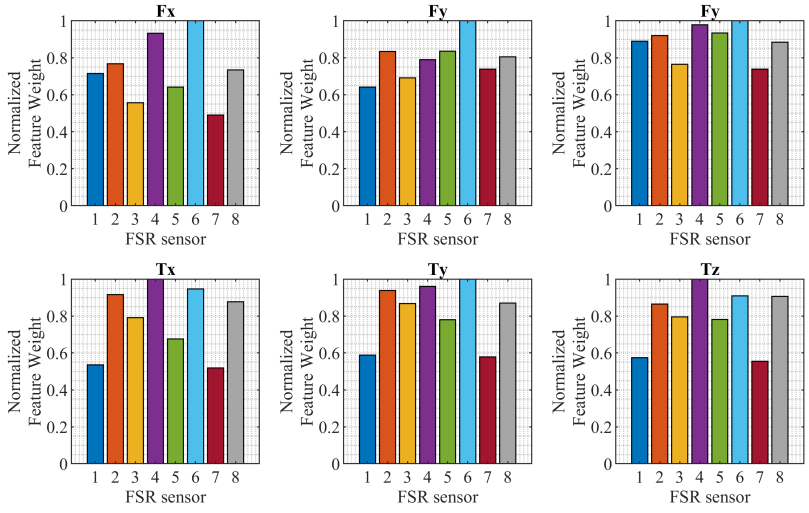

Figure 38 – Combined NCA feature selection.

second experiment was set with interaction type 4 and the misaligned 3 configuration. Figure 40 shows the regression results of these tests. The r-squared is indicated on each

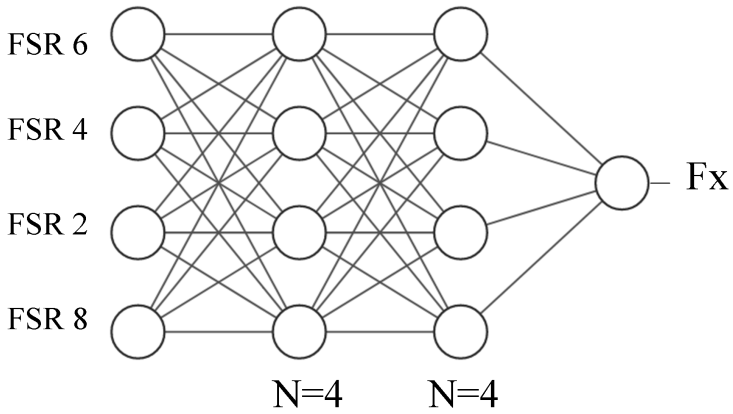

Figure 39 – Neural Network diagram for the regression of Fx.

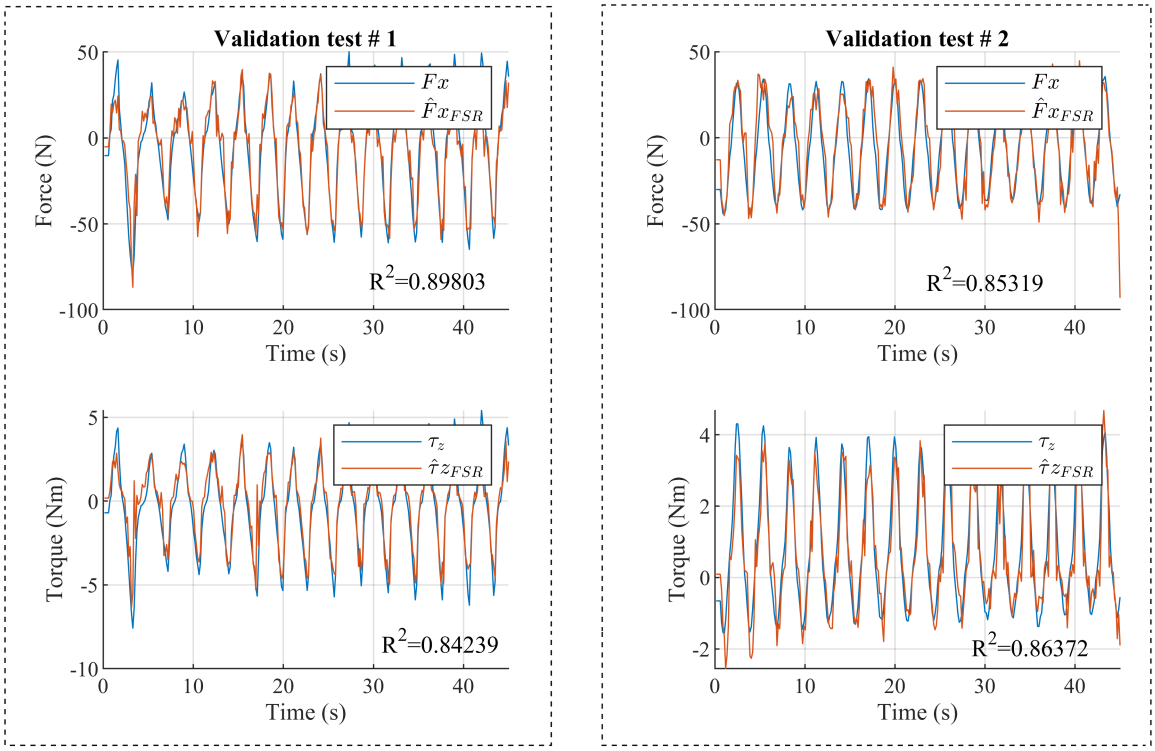

Figure 40 – Regression of Fx and Tz signals for a user in two experiments.

plot; these results were obtained from new data apart from that of the dataset training; then, all the r-squared yielded are more realistic than the obtained in simulation training, with the lower value indicating 0.84, considered an acceptable regression performance.

5.4 Human joint torque estimation

This section shows the outcomes of employing the FSR sensor array to estimate human joint torque using DO-based techniques. These findings are based on experiments conducted with the same participant and following the methodology outlined in the validation of the regression network (Section 5.3.2).

5.4.1 User participation and data collection

Five volunteers participated in the study (males, averaging 173 ± 2 cm and 65 ± 3 kg), undergoing experiments across the different misalignment configurations. The experiments aimed to mimic real-life physical interactions during collaborative tasks with the robot. Each user experienced all five misalignment configurations, and four experiment types were conducted for each configuration. Experiments were approved by the Ethics Committee of the University of São Paulo, School of Physical Education and Sport of Ribeirão Preto, EEFERP-USP, CAAE No. 41150620.7.0000.5659, decision statement No 4.579.836.

Using the setup for the rotary SEA presented in Section 2.4.2.1, four distinct types of experiments were conducted for each misalignment configuration, as outlined in Table 9. These experiments varied the robotic joint's behavior and the user's response, ranging from static to active movement engagement. The user's knee joint angle was captured in the experiments using a wearable device developed in (Jaimes; Wolschick; Siqueira, 2023), a parallel scientific contribution to this thesis. This instrumented knee brace, detailed in Appendix B, is integrated with POF and capacitive sensors to estimate knee joint angles and identify human physical activity.

Table 9 – Experiments types for HRI interaction

Interaction Type	Human Behavior	Robot Behavior
1	Active(θ_H = Flex. and Ext.)	Active ($\theta_R = 0$)
2	Active(θ_H = Flex. and Ext.)	Passive.
3	Passive	Active (θ_R = Sine).
4	Active ($\theta_H = 0$)	Active (θ_R = Sine).

5.4.2 Experimental results

Figures 41 and 42 show the time responses of all the variables involved during the experiments. The variables were segmented through a normalized time cycle, with their average values represented by solid lines and variability by shaded regions. The arrangement of the plots is as follows: The left series delineates dynamic and kinematic variables as recorded by the robotic system, including the misalignment angle φ. This angle, representing the misalignment factor, was deduced from data acquired via IMU sensors positioned in both the human limb and the robotic linkage. The central series of plots displays the data from the FSR sensor array. The concluding series on the right side displays the Force/Torque (F/T) sensor variables, providing a comprehensive view of the forces and torques emerging from the interaction. The corresponding torque estimation results for both aligned and misaligned conditions are illustrated in Figures 43 and 44, respectively.

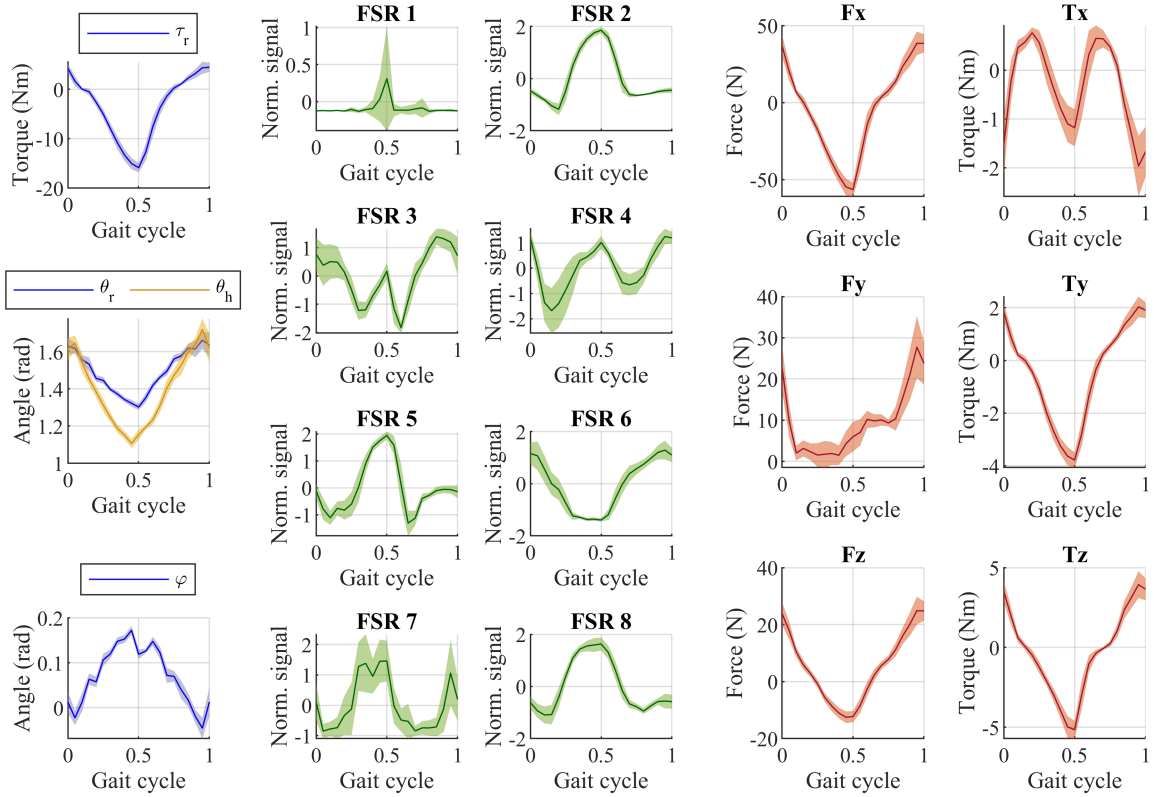

Figure 41 – Time responses for the aligned experiment

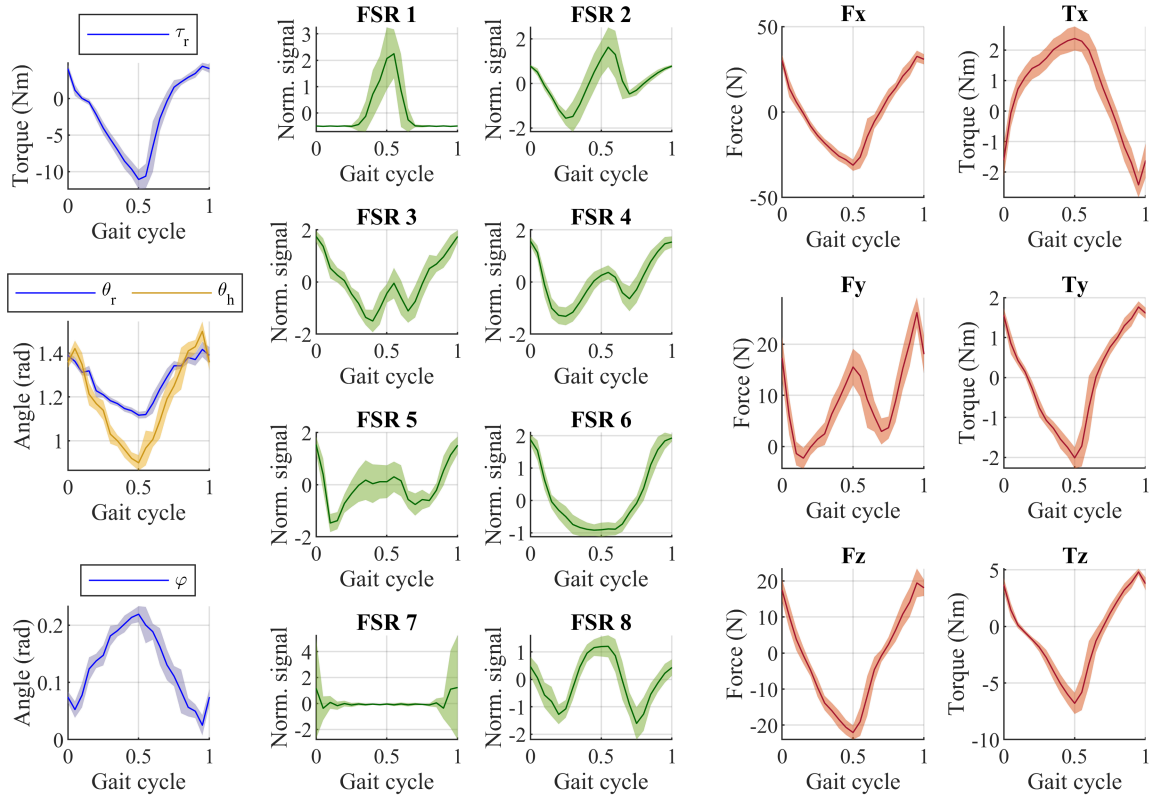

Figure 42 – Time responses for the misaligned experiment

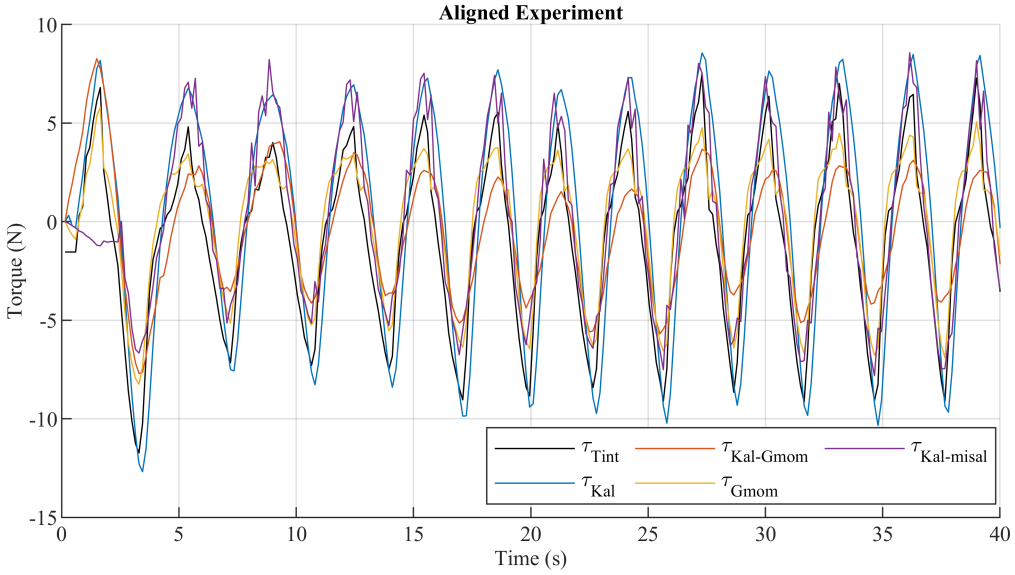

Figure 43 – Results for the alignment experiment.

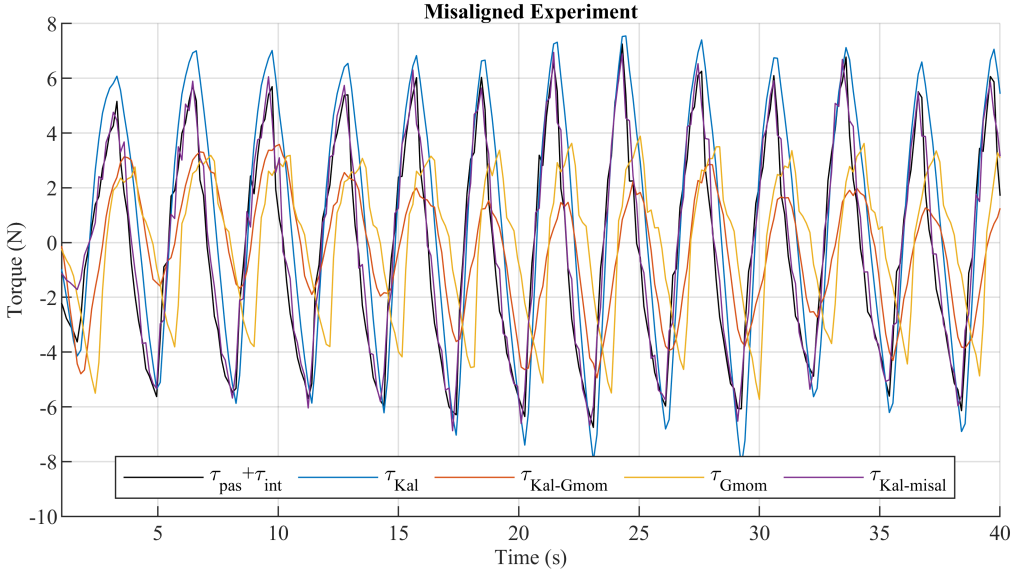

Figure 44 – Results for the misalignment experiment.

Table 10 and 11 shows the values of Root Mean Square Error (RMSE), Dynamic Time Warping index (DTW), and Time Lag (Lag) using cross-correlation for the estimated interaction torques.

Index	$\hat{\tau}_{Kal}$	$\hat{\tau}_{Kal\_Gmom}$	$\hat{\tau}_{Gmom}$	$\hat{\tau}_{Kal\_misal}$
RMSE	4.8579	4.0186	2.4239	3.6040
DTW	96.1376	26.1807	42.8009	73.5479
Time Lag	-0.1500	-0.1500	-5.5500	-0.1500

Table 10 – Performance indexes for torque estimation using the FSR array sensor for the aligned experiment case.

Index	$\hat{\tau}_{Kal}$	$\hat{\tau}_{Kal\_Gmom}$	$\hat{\tau}_{Gmom}$	$\hat{\tau}_{Kal\_misal}$
RMSE	4.8924	3.0468	2.6499	2.7371
DTW	68.4859	16.1382	27.9181	52.7404
Time Lag	-0.1500	2.5500	0.9000	0.005

Table 11 – Performance indexes for torque estimation using the FSR array sensor for the misaligned experiment case.

The Time Lag metric, across both aligned and misaligned experimental conditions, underscores the efficacy of integrating disturbance torque within state variables via Kalman filter approaches, evidenced by their minimal time lag compared to other techniques. This finding highlights the precision of Kalman filter methodologies in tracking the dynamic phases of interaction torques with negligible delay.

Moreover, the Dynamic Time Warping (DTW) analysis reveals that combining Kalman filters with generalized momentum closely mimics the target signal's dynamic behavior, achieving the most accurate representation of time series shape. On the other hand, the RMSE values indicate the signal generalized momentum as having the lowest error. This outcome emphasizes the importance of considering error magnitude and signal similarity in evaluating estimator accuracy. The DTW results particularly indicate the Kalman filter combined with the generalized momentum technique's superior ability to align with the dynamic patterns of the target series, highlighting the relevance of similarity metrics alongside traditional error measures in assessing the estimated torques.

6 CONCLUSIONS

This PhD Thesis developed methods for estimating human joint torques using Disturbance Observer (DO) based approaches and specialized HRI sensor systems. The research focused on addressing joint misalignment and human-robot interaction forces to enhance the control strategies in robotic rehabilitation, thereby improving their effectiveness, safety, and transparency.

Three specialized sensor systems were assembled to quantify joint misalignment and physical human-robot interaction. The evaluation of HRI forces using the sensor prototypes was conducted using healthy volunteers under various configurations. An important contribution of this work is the development of a modeling for HRI systems that includes joint misalignment and human-robot interaction forces. Compared with the HRI aligned model, the results of the DO-based techniques with the HRI misaligned modeling improved the precision and reliability of torque estimation.

The initial prototype employing Fiber Optic technology demonstrated high accuracy in HRI force prediction and provided insights into force distribution relative to joint misalignment. Subsequent prototypes used FSR Sensors, introducing a misalignment factor and refined measurement methodologies. The final prototype featured an array of FSR Sensors, showing more accurate torque estimation due to its tailored experimental setup for assessing misalignment effects during motion exercises.

The initial prototype, which utilized Fiber Optic technology, introduced the concept of differential measurement. It demonstrated high accuracy in predicting the HRI forces and helped to understand the force distribution and its dependency on joint misalignment. This prototype was succeeded by a similar version employing FSR Sensors and a novel misalignment factor. The final prototype featured an array of FSR Sensors, showing more accurate torque estimation due to its tailored experimental setup for assessing misalignment effects during motion exercises.

7 DISCUSSION AND FUTURE WORKS

Some limitations of the results must be addressed to improve understanding of the study's outcomes and contribute to future research directions.

The human-robot interaction modeling simplified the dynamic nature of human joint behavior by treating knee mechanical impedance parameters (inertia, damping, and stiffness) as constants. However, during activities like walking, these parameters tend to vary with gait phases. Hence, this assumption limits torque estimations' accuracy and subsequent application in robotic control. It is known that human impedance parameters exhibit time-varying characteristics that are crucial for accurate modeling during dynamic activities (Lee; Rouse; Krebs, 2016; Rouse *et al.*, 2014). The HRI nominal modeling using the ExoTAO robot used the impedance model parameters computed in (Escalante *et al.*, 2020). Similarly, for the EICoSI robot, the impedance parameters from (Rifai *et al.*, 2017) were used as a reference for the HRI nominal modeling.

The assumption of constant parameters was made to focus the research on the effects of human-robot interaction in misalignment configurations and the enhancement potential of DO-based techniques. However, for future work, incorporating time-varying impedance parameters based on empirical data from gait analysis could enhance the model's accuracy and applicability to real-world robotic control systems. Other research in our group has already addressed the time-varying modeling approach to develop robotic control techniques for gait assistance, leading to more effective and adaptive robotic assistance outcomes (Escalante *et al.*, 2018; Escalante *et al.*, 2020). Combining the research outcomes in this thesis with time-varying impedance identification will enhance control techniques and improve the understanding of human-robot interaction dynamics in misalignment configurations.

The HRI modeling assumed a fixed center of rotation, simplifying the joint's dynamics, given that the knee's axis of rotation is not fixed. Despite this simplification, the model has demonstrated effective torque estimation within the proposed robotic scenarios. It shows that accounting for misalignment, even in a simplified form, significantly enhances the accuracy of torque estimations over models that ignore misalignment altogether.

Future works will focus on developing a low-cost monitoring system to accurately track the dynamic axis of rotation for both robotic and human knee joints. This system will capture the variable nature of the knee's axis with greater precision, enhancing the model's fidelity and applicability to real robotic rehabilitation scenarios. Despite its simplicity, the current model proves that the recognition and modeling of misalignment substantially improve the theoretical and practical outcomes.

This thesis used POF sensors without applying the viscoelastic compensation techniques mentioned in (Leal-Junior *et al.*, 2018b). As a result, the inherent hysteresis effects in the polymer materials used in these sensors were not addressed. By implementing this technique, the precision of the POF sensors could be significantly improved by reducing hysteresis and improving linearity. This improvement could lead to better raw data for forecast contact forces in dynamic HRI settings. In the future, exploring this compensation approach could lead to more reliable sensor feedback.

Due to the setup created for its assessment, the FSR sensor array captured with more accuracy and flexibility the HRI interaction torques in the presence of misalignments, hence offering more reliable knee joint torque estimation. Nevertheless, far from stating the superiority of this technology, it is necessary to affirm that it was also possible to quantity joint misalignment with the other prototype setups during the experiments.

APPENDIX

APPENDIX A – METRICS FOR SIMILARITY ANALYSIS

A.1 Cross-Correlation Theory

Cross-correlation, a method extensively used in signal processing, measures the similarity between two signals as a function of a time lag applied to one of them (Gajic, 2003). Mathematically, the cross-correlation of two discrete signals $x[n]$ and $y[n]$ is defined as:

$$R_{xy}[k] = \sum_{n=-\infty}^{\infty} x[n] \cdot y[n+k] \tag{A.1}$$

The function $R_{xy}[k]$ peaks at a lag where the signals are most similar. This method is especially useful in identifying the time offset between similar signals in various applications.

A.2 Dynamic Time Warping Index

Dynamic Time Warping (DTW) is an algorithm particularly effective for measuring similarity between two temporal sequences, which may vary in time or speed (Senin, 2008; Tavenard, 2021). For two sequences $X = \{x_1, x_2, ..., x_M\}$ and $Y = \{y_1, y_2, ..., y_N\}$, the DTW distance is computed as follows:

$$DTW(X,Y) = \sqrt{d(M,N)} \tag{A.2}$$

where $d(i,j)$ is typically the squared difference between x_i and y_j:

$$d(i,j) = (x_i - y_j)^2 \tag{A.3}$$

The DTW algorithm uses dynamic programming to compute this distance, creating an $M \times N$ matrix where each element $d(i,j)$ represents the distance between x_i and y_j. The optimal path through this matrix minimizes the cumulative distance and represents the best alignment between the sequences.

The DTW algorithm can be summarized as follows (Senin, 2008):

1. Initialize a matrix D of size $M \times N$ with high values.
2. Set $D(0,0)$ to 0.
3. For each element (i,j) in D, calculate $d(i,j)$ and update $D(i,j)$ as:

$$D(i,j) = d(i,j) + \min(D(i-1,j-1), D(i-1,j), D(i,j-1)) \tag{A.4}$$

4. The DTW distance is $D(M, N)$, the bottom right corner of the matrix.

Time Lag using Cross-correlation and DTW are complementary in signal analysis. While cross-correlation is adept at detecting linear similarities and alignment, DTW focuses on measuring the similarity between sequences with temporal variations, making it suitable for complex signal comparisons in dynamic environments.

A.3 Neighborhood Component Analysis for Regression

Neighborhood Component Analysis (NCA) for regression is a technique that focuses on enhancing the predictive accuracy of models by identifying the most significant features. Originating in classification, its principles have been adapted for regression, prioritizing influential features through weight allocation (Yang; Laaksonen, 2007). This process reduces the influence of less pertinent attributes, refining the model's predictive capabilities by selecting optimal feature weights.

NCA applies a transformation matrix, denoted as A, to project data x_i into a dimensionally reduced space. This projection aims to optimize the Leave-One-Out (LOO) criterion for the k-nearest neighbors algorithm, utilizing a probabilistic approach for neighbor relations in the transformed domain:

$$p_{ij} = \frac{\exp(-\|Ax_i - Ax_j\|^2)}{\sum_{k \neq i} \exp(-\|Ax_i - Ax_k\|^2)}, \quad p_{ii} = 0. \tag{A.5}$$

The cumulative probability p_i, summing over all instances sharing the same class label, is given by:

$$p_i = \sum_{j:c_i=c_j} p_{ij}. \tag{A.6}$$

Consequently, NCA's objective is defined as the maximization problem:

$$J_{\mathrm{NCA}}(A) = \sum_{i=1}^{n} p_i. \tag{A.7}$$

The learning process for NCA involves optimizing A via its gradient:

$$\frac{\partial J_{\mathrm{NCA}}(A)}{\partial A} = 2A \sum_{i=1}^{n} \left(p_i \sum_{k=1}^{n} p_{ik} x_{ik} x_{ik}^T - \sum_{j:c_i=c_j} p_{ij} x_{ij} x_{ij}^T \right). \tag{A.8}$$

An optimization algorithm such as conjugate gradients is typically employed to refine the matrix A.

APPENDIX B – WEARABLE DEVICE FOR HUMAN KNEE ANGLE AND PHYSICAL ACTIVITY ESTIMATION

Adequate physical activity monitoring is essential for people's quality of life and health, helping to assess gait, balance, fall prevention, pattern recognition and monitoring of neurological diseases. Wearable devices with inertial sensors (IMUs) and resistive force sensors (RSFs) have been widely used to measure kinematic and dynamic signals in gait analysis, helping therapists plan and evaluate rehabilitation activities. (Wind *et al.*, 2009). However, challenges such as processing time, sensor fixation, calibration and durability persist (Seel; Kok; McGinnis, 2020; Swanson *et al.*, 2019), motivating the development of new technologies based on *soft sensors* (Amjadi *et al.*, 2016; Vargas-Valencia *et al.*, 2021), which are built with biocompatible materials, providing soft, elastic and deformable systems. This paper presents an innovative wearable sensory system to monitor human physical activity, using soft capacitive bending sensors and polymer fiber optics to estimate knee angles and classify the type of physical activity. The proposed system addresses cost and accuracy limitations of commercial devices, contributing to the development of more affordable and efficient technologies in physical activity monitoring.

The proposed wearable system for monitoring human physical activity, as shown in Figure 45, uses soft sensors to estimate knee joint angles and identify the type of physical activity performed. These sensors are positioned. The system integrates a microcontroller for data acquisition and processing, this module is responsible for collecting, segmenting and sending the data in real time via Bluetooth to a computer where machine learning algorithms are implemented.

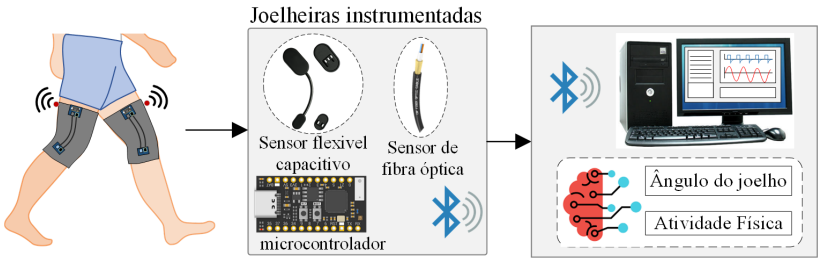

Figure 45 – Wearable sensor system proposed for monitoring physical activity

The proposed system uses two types of bending sensors. The first is the BendLabs two-axis flexible bidirectional capacitive sensor, a lightweight, multidirectional sensor for bending angle measurement. It measures two angles in orthogonal planes for 3D orientation and detects angular deformations in the XY and XZ planes. The sensor contains two voltage-sensitive capacitors, and when deflected, the difference in capacitance of the inner and outer capacitors is linearly proportional to the deflection angle (see Figure 46a). The sensor has an I2C communication interface, operates at a frequency of 200Hz and its

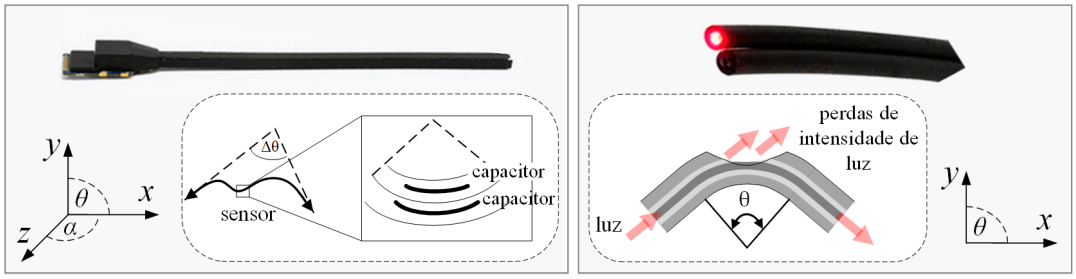

(a) (b)

Figure 46 – Hardware and operating principle of sensors used in the monitoring system. (a) BendLabs two-axis flexible bidirectional sensor. (b) PMMA multi-mode polymer fiber.

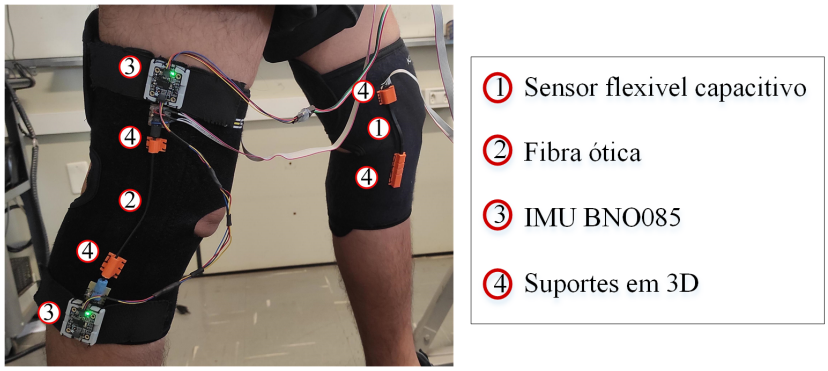

Figure 47 – Experimental set-up of the wearable system.

repeatability is 0.18 °. The second type of sensor is based on PMMA multimode polymer fiber, which has a core diameter of 980 μm and a cladding thickness of 10 μm (Eska, 2024). This type of sensor has been used in assistive technologies (G. *et al.*, 2019). The fiber's light power is transmitted through its core and suffers attenuation when the fiber is bent (Figure 46b). This attenuation or loss can be measured and is associated with the signal from the physical source causing such bending, for example, angle.

Neoprene orthopedic knee pads attach the sensors to the knee joints. The knee pads and sensors were assembled experimentally as shown in Figure 47. Additive manufacturing (3D printing) parts were developed and sewn into the correct positions to ensure proper alignment and fixation.

B.1 Experimental Results

BNO085 inertial sensors were added to the experimental setup to train the estimation algorithms with a real knee angle reference. These sensors were positioned on the thigh and shin of each leg, and the Euler angles were calculated using quaternions, with θ being the angle in the sagittal plane:

$$\theta = \arctan\left(\frac{2(q_0 q_1 + q_2 q_3)}{1 - 2(q_1^2 + q_2^2)}\right) \tag{B.1}$$

B.1.1 Data Collection

To conduct a preliminary data analysis, a test protocol was drawn up to be applied to six healthy volunteer users. In this protocol, each participant defined and performed three different types of activities twice. The data was collected and recorded in a database. Table 12 gives an overview of the test protocol adopted.

Type of activity	Description	Duration of test
1	Walk slowly at 1 m/s	30 s
2	Walk fast at 2 m/s	30 s
3	Sit and stand	5 repetitions

Table 12 – Experimental protocol for data collection

Data was collected by repeating the protocol once for each user, totaling six sets per user. Figure 48 illustrates the data collected from the right knee pad during a specific test of the experimental protocol, in which a participant walked on a treadmill at 1 m/s for 30 seconds wearing the instrumented knee pads. In the Figure, the raw data obtained by the sensors is compared with the angle of the IMUs, the subplot above shows the data from the fiber optic sensor and the middle subplot shows the signals from the flexible capacitive sensor representing the bending angles in degrees in the XY and XZ planes. The third subplot shows the relative knee angle signal calculated by the IMUs.

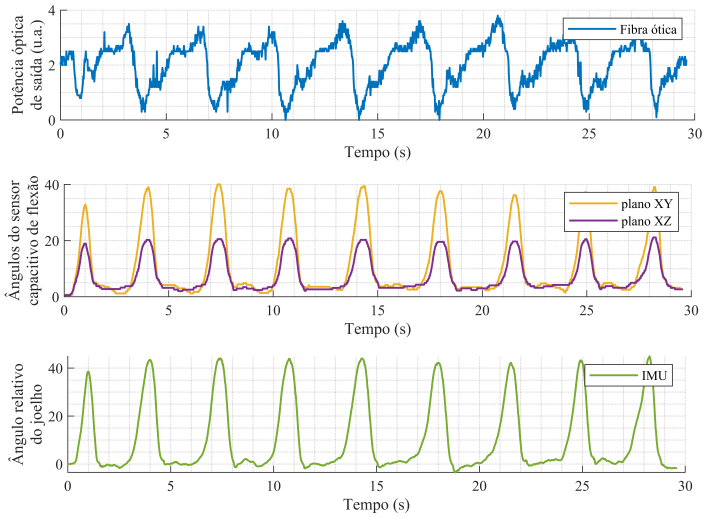

Figure 48 – IMU, capacitive flex sensors and POF values for the right leg

B.1.2 Knee Angle Estimation

The MLP neural network was used to estimate the knee angle, with different architectures for each set of knee pads. The training resulted in an accuracy of 98.1% and 98.8% for the left and right legs, respectively. Figure 49 shows the estimation results for

one of the evaluation tests, in this case, the right knee angle of a user performing activity 3, sitting and standing.

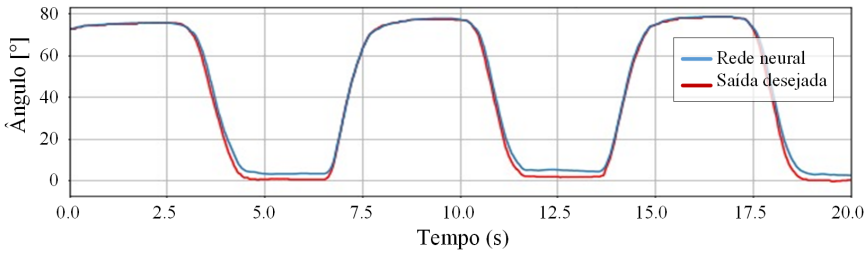

Figure 49 – Neural network output results and reference signal

REFERENCES

Abhishek, G.; K., O. M. Disturbance-observer-based force estimation for haptic feedback. **Journal of Dynamic Systems, Measurement, and Control**, v. 133, n. 1, Dec 2010.

Aguirre-Ollinger, G. *et al.* Active-impedance control of a lower-limb assistive exoskeleton. *In*: **2007 IEEE 10th International Conference on Rehabilitation Robotics**. [*S.l.: s.n.*], 2007. p. 188–195.

Amjadi, M. *et al.* Stretchable, skin-mountable, and wearable strain sensors and their potential applications: a review. **Advanced Functional Materials**, Wiley Online Library, v. 26, n. 11, p. 1678–1698, 2016.

Bessler-Etten, J. *et al.* Investigating change of discomfort during repetitive force exertion though an exoskeleton cuff. **Applied Ergonomics**, v. 115, p. 104055, 2024. ISSN 0003-6870. Disponível em: https://www.sciencedirect.com/science/article/pii/S0003687023000935.

Bessler, J. *et al.* Prototype measuring device for assessing interaction forces between human limbs and rehabilitation robots - a proof of concept study. *In*: **2019 IEEE 16th International Conference on Rehabilitation Robotics (ICORR)**. [*S.l.: s.n.*], 2019. p. 1109–1114.

Calanca, A.; Capisani, L.; Fiorini, P. Robust force control of series elastic actuators. **Actuators**, v. 3, n. 3, p. 182–204, 2014. ISSN 2076-0825.

Calanca, A.; Fiorini, P. Human-adaptive control of series elastic actuators. **Robotica**, Cambridge University Press, v. 32, n. 8, p. 1301–1316, 2014.

Chander, D. S. *et al.* A comparison of different methods for modelling the physical human-exoskeleton interface. **International Journal of Human Factors Modelling and Simulation**, v. 7, n. 3-4, p. 204–230, 2022. Disponível em: https://www.inderscienceonline.com/doi/abs/10.1504/IJHFMS.2022.124310.

Chen, W.-H. *et al.* A nonlinear disturbance observer for robotic manipulators. **IEEE Transactions on Industrial Electronics**, v. 47, n. 4, p. 932–938, 2000.

Daud, O. *et al.* Development of a four-channel haptic system for remote assessment of patients with impaired hands. **Robotica**, Cambridge University Press, v. 35, n. 10, p. 1975–1991, 2017.

Dautenhahn, K. Robots in the wild: Exploring human–robot interaction in naturalistic environments. **Interaction Studies**, John Benjamins, v. 10, n. 3, p. 269–273, 2009. ISSN 1572-0373. Disponível em: https://www.jbe-platform.com/content/journals/10.1075/is.10.3.01dau.

De Luca, A. *et al.* Collision detection and safe reaction with the dlr-iii lightweight manipulator arm. *In*: **2006 IEEE/RSJ International Conference on Intelligent Robots and Systems**. [*S.l.: s.n.*], 2006. p. 1623–1630.

de Luca, A.; Mattone, R. Sensorless robot collision detection and hybrid force/motion control. *In*: **Proceedings of the 2005 IEEE International Conference on Robotics and Automation**. [*S.l.: s.n.*], 2005. p. 999–1004.

Dezman, M. *et al.* A mechatronic leg replica to benchmark human–exoskeleton physical interactions. **Bioinspiration & Biomimetics**, IOP Publishing, v. 18, n. 3, p. 036009, apr 2023. Disponível em: https://dx.doi.org/10.1088/1748-3190/accda8.

Dianchun, B. *et al.* 3d contact force sensor for assisted rehabilitation robot human-computer interaction. *In*: **Proceeding of the 11th World Congress on Intelligent Control and Automation**. [*S.l.: s.n.*], 2014. p. 2804–2807.

dos Santos, W. M.; Caurin, G. A.; Siqueira, A. A. Design and control of an active knee orthosis driven by a rotary series elastic actuator. **Control Engineering Practice**, v. 58, p. 307 – 318, 2017. ISSN 0967-0661.

dos Santos, W. M.; Siqueira, A. A. G. Design and control of a transparent lower limb exoskeleton. *In*: CARROZZA, M. C.; MICERA, S.; PONS, J. L. (ed.). **Wearable Robotics: Challenges and Trends**. Cham: Springer International Publishing, 2019. p. 175–179. ISBN 978-3-030-01887-0.

dos Santos, W. M.; Siqueira, A. A. G. Optimal impedance via model predictive control for robot-aided rehabilitation. **Control Engineering Practice**, v. 93, p. 104177, Dec 2019. ISSN 0967-0661.

Erwin, A. *et al.* Interaction control for rehabilitation robotics via a low-cost force sensing handle. *In*: . [*S.l.: s.n.*], 2013.

Escalante, F. M. *et al.* Robust kalman filter and robust regulator for discrete-time Markovian jump linear systems: Control of series elastic actuators. *In*: **2018 IEEE Conference on Control Technology and Applications (CCTA)**. [*S.l.: s.n.*], 2018. p. 976–981.

Escalante, F. M. *et al.* Robust markovian impedance control applied to modular knee-exoskeleton. **IFAC-PapersOnLine**, v. 53, n. 2, p. 10141–10147, 2020. ISSN 2405-8963. 21st IFAC World Congress. Disponível em: https://www.sciencedirect.com/science/article/pii/S2405896320335035.

Escalante, F. M. *et al.* Markovian transparency control of an exoskeleton robot. **IEEE Robotics and Automation Letters**, v. 8, n. 2, p. 544–551, 2023.

Eska, M. **Premier Simplex Optical Fiber Cable**. 2024. https://fiberfin.com/product/ff-gh-4001-p/. Acess: 2024-01-02.

Esmaeili, M. *et al.* Ergonomic considerations for anthropomorphic wrist exoskeletons: A simulation study on the effects of joint misalignment. *In*: **2011 IEEE/RSJ International Conference on Intelligent Robots and Systems**. [*S.l.: s.n.*], 2011. p. 4905–4910.

G., L. A. *et al.* Polymer optical fiber sensors in healthcare applications: A comprehensive review. **Sensors**, v. 19, n. 14, 2019. ISSN 1424-8220. Disponível em: https://www.mdpi.com/1424-8220/19/14/3156.

Gajic, Z. **Linear Dynamic Systems and Signals**. Prentice Hall/Pearson Education, 2003. ISBN 9780201618549. Disponível em: https://books.google.com.co/books?id=yOhiQgAACAAJ.

Gordon, D. F. N.; Henderson, G.; Vijayakumar, S. Effectively quantifying the performance of lower-limb exoskeletons over a range of walking conditions. **Frontiers in Robotics and AI**, v. 5, 2018. ISSN 2296-9144. Disponível em: https://www.frontiersin.org/articles/10.3389/frobt.2018.00061.

Grosu, V. *et al.* Multi-axis force sensor for human–robot interaction sensing in a rehabilitation robotic device. **Sensors (Basel, Switzerland)**, v. 17, 2017. ISSN 1424-8220.

Gui, K.; Liu, H.; Zhang, D. Toward multimodal human–robot interaction to enhance active participation of users in gait rehabilitation. **IEEE Transactions on Neural Systems and Rehabilitation Engineering**, v. 25, n. 11, p. 2054–2066, 2017.

Huang, J. *et al.* Control of upper-limb power-assist exoskeleton using a human-robot interface based on motion intention recognition. **IEEE Transactions on Automation Science and Engineering**, v. 12, n. 4, p. 1257–1270, 2015.

Huo, W. *et al.* Control of a rehabilitation robotic exoskeleton based on intentional reaching direction. *In*: **2010 International Symposium on Micro-NanoMechatronics and Human Science**. [*S.l.: s.n.*], 2010. p. 357–362.

Huo, W.; Mohammed, S.; Amirat, Y. Impedance reduction control of a knee joint human-exoskeleton system. **IEEE Transactions on Control Systems Technology**, v. 27, n. 6, p. 2541–2556, Nov 2019. ISSN 2374-0159.

Jaimes, J. C. **Ankle torque estimation for lower-limb robotic rehabilitation**. 2018. Dissertação (Mestrado) — Universidade de São Paulo, 2018.

Jaimes, J. C.; Wolschick, G. d. O.; Siqueira, A. A. G. Sistema vestível para monitoramento da atividade física. *In*: **XII Congreso Iberoamericano de Tecnologías de Apoyo a la Discapacidad IBERDISCAP2023**. [*S.l.: s.n.*]: AITADIS, 2023. Paper accepted for presentation.

Javaid, U. *et al.* Observer-based attitude control of spacecraft under actuator dead zone and misalignment faults. **Applied Mathematics and Computation**, v. 465, p. 128406, 2024. ISSN 0096-3003. Disponível em: https://www.sciencedirect.com/science/article/pii/S0096300323005751.

Jutinico, A. L. *et al.* Impedance control for robotic rehabilitation: A robust Markovian approach. **Frontiers in Neurorobotics**, v. 11, p. 43, August 2017. ISSN 1662-5218.

Kasi, V. *et al.* Robotic system development for cooperative orthopedic drilling assistance. **Advances in Mechanical Engineering**, v. 6, p. 437485, 2014. Disponível em: https://doi.org/10.1155/2014/437485.

Koller, J. *et al.* 'body-in-the-loop' optimization of assistive robotic devices: A validation study. *In*: **Robotics: Science and Systems**. [*S.l.: s.n.*], 2016.

Kristensen, O. H.; Stenager, E.; Dalgas, U. Muscle strength and poststroke hemiplegia: A systematic review of muscle strength assessment and muscle strength impairment. **Archives of Physical Medicine and Rehabilitation**, v. 98, n. 2, p. 368 – 380, 2017. ISSN 0003-9993.

Kuan, J.; Huang, T.; Huang, H. Human intention estimation method for a new compliant rehabilitation and assistive robot. *In*: **Proceedings of SICE Annual Conference 2010**. [*S.l.: s.n.*], 2010. p. 2348–2353.

Leal-Junior, A. G. *et al.* Polymer optical fiber-based integrated instrumentation in a robot-assisted rehabilitation smart environment: A proof of concept. **Sensors**, v. 20, n. 11, 2020. ISSN 1424-8220. Disponível em: https://www.mdpi.com/1424-8220/20/11/3199.

Leal-Junior, A. G. *et al.* 3d-printed pof insole: Development and applications of a low-cost, highly customizable device for plantar pressure and ground reaction forces monitoring. **Optics & Laser Technology**, v. 116, p. 256 – 264, 2019. ISSN 0030-3992.

Leal-Junior, A. G. *et al.* Polymer optical fiber-embedded, 3d-printed instrumented support for microclimate and human-robot interaction forces assessment. **Optics & Laser Technology**, v. 112, p. 323 – 331, 2019. ISSN 0030-3992.

Leal-Junior, A. G. *et al.* Polymer optical fiber for in-shoe monitoring of ground reaction forces during the gait. **IEEE Sensors Journal**, v. 18, n. 6, p. 2362–2368, 2018.

Leal-Junior, A. G. *et al.* Viscoelastic features based compensation technique for polymer optical fiber curvature sensors. **Optics & Laser Technology**, v. 105, p. 35–40, 2018. ISSN 0030-3992. Disponível em: https://www.sciencedirect.com/science/article/pii/S0030399217315566.

Leal Junior, A. G.; Frizera, A.; Pontes, M. J. Analytical model for a polymer optical fiber under dynamic bending. **Optics & Laser Technology**, v. 93, p. 92 – 98, 2017. ISSN 0030-3992.

Lee, H.; Rouse, E. J.; Krebs, H. I. Summary of human ankle mechanical impedance during walking. **IEEE Journal of Translational Engineering in Health and Medicine**, v. 4, p. 1–7, Sept 2016. ISSN 2168-2372.

Lenzi, T. *et al.* Intention-based emg control for powered exoskeletons. **IEEE Transactions on Biomedical Engineering**, v. 59, n. 8, p. 2180–2190, Aug 2012. ISSN 0018-9294.

Lenzi, T. *et al.* Measuring human–robot interaction on wearable robots: A distributed approach. **Mechatronics**, v. 21, n. 6, p. 1123 – 1131, 2011. ISSN 0957-4158.

Lunenburger, G.; Colombo, G.; Riener, R. Biofeedback for robotic gait rehabilitation. **Journal of NeuroEngineering and Rehabilitation**, v. 4, n. 1, p. 1, 2007. ISSN 1743-0003.

Mallat, R. *et al.* Human-exoskeleton joint misalignment: A systematic review. *In*: **2019 Fifth International Conference on Advances in Biomedical Engineering (ICABME)**. [*S.l.: s.n.*], 2019. p. 1–4.

Mohammed, S. *et al.* Nonlinear disturbance observer based sliding mode control of a human-driven knee joint orthosis. **Robotics and Autonomous Systems**, v. 75, p. 41 – 49, 2016. ISSN 0921-8890. Assistance and Service Robotics in a Human Environment.

Moreno, J. *et al.* Wearable robot technologies. **Wearable robots: biomechatronic exoskeletons. Hoboken: John Wiley & Sons**, p. 165–99, 2008.

Ohnishi, K. A new servo method in mechatronics. *In*: **Transactions of Japanese Society of Electrical Engineers**. [*S.l.: s.n.*], 1987. v. 107 n.3, p. 83–86.

PETERS, K. Polymer optical fiber sensors—a review. **Smart Materials and Structures**, IOP Publishing, v. 20, n. 1, p. 013002, dec 2010. Disponível em: https://doi.org/10.1088/0964-1726/20/1/013002.

Rahuman, M. A. A. *et al.* Recent technological progress of fiber-optical sensors for bio-mechatronics applications. **Technologies**, v. 11, n. 6, 2023. ISSN 2227-7080. Disponível em: https://www.mdpi.com/2227-7080/11/6/157.

Rathore, A. *et al.* Quantifying the human-robot interaction forces between a lower limb exoskeleton and healthy users. *In*: **2016 38th Annual International Conference of the IEEE Engineering in Medicine and Biology Society (EMBC)**. [*S.l.: s.n.*], 2016. p. 586–589.

Rifai, H. *et al.* Toward lower limbs functional rehabilitation through a knee-joint exoskeleton. **IEEE Transactions on Control Systems Technology**, v. 25, n. 2, p. 712–719, March 2017. ISSN 1063-6536.

Rouse, E. J. *et al.* Estimation of human ankle impedance during the stance phase of walking. **IEEE Transactions on Neural Systems and Rehabilitation Engineering**, v. 22, n. 4, p. 870–878, July 2014. ISSN 1534-4320.

S, G. M.; Angus, A. P. **Kalman filtering: Theory and Practice with MATLAB**. [*S.l.: s.n.*]: John Wiley & Sons, 2014.

Sabanovic, A.; Ohnishi, K. **Motion control systems**. [*S.l.: s.n.*]: John Wiley & Sons, 2011.

Schiele, A. An explicit model to predict and interpret constraint force creation in phri with exoskeletons. *In*: **2008 IEEE International Conference on Robotics and Automation**. [*S.l.: s.n.*], 2008. p. 1324–1330.

Seel, T.; Kok, M.; McGinnis, R. S. Inertial sensors—applications and challenges in a nutshell. **Sensors**, v. 20, n. 21, 2020. ISSN 1424-8220. Disponível em: https://www.mdpi.com/1424-8220/20/21/6221.

Senin, P. Dynamic time warping algorithm review. **Information and Computer Science Department University of Hawaii at Manoa Honolulu, USA**, v. 855, n. 1-23, p. 40, 2008.

Sheridan, T. B. Human–robot interaction: Status and challenges. **Human Factors**, v. 58, n. 4, p. 525–532, 2016. PMID: 27098262. Disponível em: https://doi.org/10.1177/0018720816644364.

Staudenmann, D. *et al.* Methodological aspects of semg recordings for force estimation – a tutorial and review. **Journal of Electromyography and Kinesiology**, v. 20, n. 3, p. 375 – 387, 2010. ISSN 1050-6411.

Sun, J.; Shen, Y.; Rosen, J. Sensor reduction, estimation, and control of an upper-limb exoskeleton. **IEEE Robotics and Automation Letters**, v. 6, n. 2, p. 1012–1019, 2021.

Swanson, E. C. *et al.* Evaluation of force sensing resistors for the measurement of interface pressures in lower limb prosthetics. **Journal of Biomechanical Engineering**, American Society of Mechanical Engineers Digital Collection, v. 141, n. 10, 2019.

Tavenard, R. **An introduction to Dynamic Time Warping**. 2021. https://rtavenar.github.io/blog/dtw.html. Accessed: 2024-01-12.

Ugurlu, B. *et al.* Proof of concept for robot-aided upper limb rehabilitation using disturbance observers. **IEEE Transactions on Human-Machine Systems**, v. 45, n. 1, p. 110–118, Feb 2015. ISSN 2168-2291.

Van Damme, M. *et al.* Estimating robot end-effector force from noisy actuator torque measurements. *In*: **2011 IEEE International Conference on Robotics and Automation**. [*S.l.: s.n.*], 2011. p. 1108–1113.

Vargas-Valencia, L. S. *et al.* Sleeve for knee angle monitoring: An imu-pof sensor fusion system. **IEEE Journal of Biomedical and Health Informatics**, v. 25, n. 2, p. 465–474, 2021.

Wahrburg, A.; Matthias, B.; Ding, H. Cartesian contact force estimation for robotic manipulators - a fault isolation perspective. **IFAC-PapersOnLine**, v. 48, n. 21, p. 1232 – 1237, 2015. ISSN 2405-8963. 9th IFAC Symposium on Fault Detection, Supervision and Safety for Technical Processes SAFEPROCESS 2015.

Wind, H. *et al.* Effect of functional capacity evaluation information on the judgment of physicians about physical work ability in the context of disability claims. **International archives of occupational and environmental health**, Springer, v. 82, n. 9, p. 1087–1096, 2009.

Yang, Z.; Laaksonen, J. Regularized neighborhood component analysis. *In*: SPRINGER. **Image Analysis: 15th Scandinavian Conference, SCIA 2007, Aalborg, Denmark, June 10-14, 2007 15**. [*S.l.: s.n.*], 2007. p. 253–262.

Zacharaki, A. *et al.* Safety bounds in human robot interaction: A survey. **Safety Science**, v. 127, p. 104667, 2020. ISSN 0925-7535. Disponível em: https://www.sciencedirect.com/science/article/pii/S0925753520300643.

Zanotto, D. *et al.* Knee joint misalignment in exoskeletons for the lower extremities: Effects on user's gait. **IEEE Transactions on Robotics**, v. 31, n. 4, p. 978–987, 2015.

Zhang, J. *et al.* Human-in-the-loop optimization of exoskeleton assistance during walking. **Science**, American Association for the Advancement of Science, v. 356, n. 6344, p. 1280–1284, 2017. ISSN 0036-8075. Disponível em: https://science.sciencemag.org/content/356/6344/1280.


EESC • USP